

## THE IMPLICATIONS OF 3D THERMAL STRUCTURE ON 1D ATMOSPHERIC RETRIEVAL

JASMINA BLECIC<sup>1,2</sup>, IAN DOBBS-DIXON<sup>1,2</sup>, THOMAS GREENE<sup>3</sup>

<sup>1</sup> NYU Abu Dhabi, Abu Dhabi, UAE

<sup>2</sup> Max-Planck-Institut für Astronomie, Königstuhl 17, D-69117 Heidelberg, Germany and

<sup>3</sup> NASA Ames Research Center, Space Science and Astrobiology Division, M.S. 245-6; Moffett Field, CA 94035, USA

Published in *ApJ*. 2017 October 23, 848:127 (24pp)

### ABSTRACT

Using the atmospheric structure from a 3D global radiation-hydrodynamic simulation of HD 189733b and the open-source Bayesian Atmospheric Radiative Transfer (BART) code, we investigate the difference between the secondary-eclipse temperature structure produced with a 3D simulation and the best-fit 1D retrieved model. Synthetic data are generated by integrating the 3D models over the *Spitzer*, the *Hubble Space Telescope (HST)*, and the *James Web Space Telescope (JWST)* bandpasses, covering the wavelength range between 1 and 11  $\mu\text{m}$  where most spectroscopically active species have pronounced features. Using the data from different observing instruments, we present detailed comparisons between the temperature–pressure profiles recovered by BART and those from the 3D simulations. We calculate several averages of the 3D thermal structure and explore which particular thermal profile matches the retrieved temperature structure. We implement two temperature parameterizations that are commonly used in retrieval to investigate different thermal profile shapes. To assess which part of the thermal structure is best constrained by the data, we generate contribution functions for both our theoretical model and each of our retrieved models. Our conclusions are strongly affected by the spectral resolution of the instruments included, their wavelength coverage, and the number of data points combined. We also see some limitations in each of the temperature parameterizations, as they are not able to fully match the complex curvatures that are usually produced in hydrodynamic simulations. The results show that our 1D retrieval is recovering a temperature and pressure profile that most closely matches the arithmetic average of the 3D thermal structure. When we use a higher resolution, more data points, and a parametrized temperature profile that allows more flexibility in the middle part of the atmosphere, we find a better match between the retrieved temperature and pressure profile and the arithmetic average. The *Spitzer* and *HST* simulated observations sample deep parts of the planetary atmosphere and provide fewer constraints on the temperature and pressure profile, while the *JWST* observations sample the middle part of the atmosphere, providing a good match with the middle and most complex part of the arithmetic average of the 3D temperature structure.

*Subject headings:* methods: numerical – planets and satellites: atmospheres – planets and satellites: composition – planets and satellites: gaseous planets – planets and satellites: individual (HD 189733b)

### 1. INTRODUCTION

Well known from our own solar system planets and general circulation models, planetary atmospheres are inherently 3D. The complex network of atmospheric dynamics, chemistry, planetary rotation, circulation, and stellar irradiation drives the planetary atmospheres to form non-uniform temperature, chemical, and cloud structures not just in the vertical direction, but also in the longitudinal and latitudinal directions (e.g., Showman et al. 2009, Dobbs-Dixon & Agol 2013).

To compare 1D models with observations, one can use self-consistent theory-driven forward models (e.g., Fortney et al. 2005, 2006, Burrows et al. 2006, Knutson et al. 2007) or observation-driven retrieval models (Madhusudhan & Seager 2009, Line et al. 2014, Waldmann et al. 2015, Blecic 2016). In general, forward techniques try to include all known physical and chemical processes to describe atmospheric thermal structure and chemical composition. Retrieval techniques, on the other hand, disfavor complex, time-consuming model calculations because of their computationally demanding iterative-statistical approach. Thus, one has to use simplified parametrized approaches that can mimic a wide variety of possible physical and chemical scenarios. In order

to constrain model parameters with the observations, the forward approach must choose a limited set of tuning parameters and fix the remaining parameters. The retrieval approach, on the other hand, performs robust exploration of the parameter phase space using statistical algorithms (Madhusudhan & Seager 2010, Benneke & Seager 2012, Lee et al. 2012, Line et al. 2014, Benneke 2015).

The complexity of these models is largely determined by the nature of the data at hand. For the low-resolution disk-integrated spectra usually observed today, the initial assumption of a 1D temperature and pressure profile and chemical composition seems to be appropriate (Swain et al. 2013, Burrows 2014, Hansen et al. 2014, Laughlin & Lissauer 2015). In addition, only a few data points are usually gathered during these observations, which further limits the complexity of the retrieved model.

With the spectral resolution and coverage of current space telescopes, one has to be careful not to overinterpret the broadband emission spectra, claiming molecular bands rather than the astrophysical and instrumental noise (Burrows 2014). However, with the advent of new spectral instruments, particularly the *James Web Space Telescope (JWST)*, our prospects of performing detailed atmospheric characterization are more promising, raising the question of whether simplified assump-

tions like 1D thermal and chemical profiles have become inadequate.

In this paper, we investigate how well these planet-averaged assumptions correspond to the realistically complex atmospheric dynamics and chemistry. To our knowledge, this is the first exploration of the limitations of 1D atmospheric retrieval that concentrates on assessing how well the reverse approach can retrieve the inherently 3D temperature structure during secondary eclipse. A recent paper from Feng *et al.* (2016) does investigate biases that result from 1D assumptions within retrieval, but they use two thermal profiles and study how non-isotropic temperature distributions can impact retrieval results. Here, we use a complex 3D thermal structure that comes from a hydrodynamic solution to generate a high-resolution model. By simulating different observing instruments, we generate data points with uncertainties and pass them to retrieval. We then explore which particular temperature profile is revealed by the retrieval using different data sets. We discuss which results are produced with the currently available and future instruments, and in particular, how well the *JWST* spectra will constrain the temperature and pressure profiles and the chemical composition of transiting exoplanets.

The paper is organized as follows: in Section 2 we describe the method and tools used in this analysis; in Section 3, we present our high-resolution synthetic model; in Section 4 we describe the retrieval setup, two temperature parametrizations, and the approach we use to average the initial 3D thermal structure and contribution functions so we can compare them with the retrieval output; in Section 5 we show results of our retrieval analyses using *JWST* data set alone and combined data sets of the *HST* and *Spitzer* and discuss their implications. In Section 6 we state our conclusions and describe the reproducible-research license (RR) that accompanies the software developed for this analysis. We also provide the webpage with the code, results, and plots produced for this paper ([github.com/dzesmin/RRC-BlecicEtal-2017-ApJ-3Dretriev](https://github.com/dzesmin/RRC-BlecicEtal-2017-ApJ-3Dretriev)). In Appendix A we explore possible thermal shapes of the two temperature parametrizations commonly used in retrieval, and in Appendix B we present our retrieval results using all simulated data sets together and each of the data sets separately.

## 2. METHOD

We use the output of our 3D radiative-hydrodynamic simulation of HD 189733b (Dobbs-Dixon & Agol 2013) to produce a high-resolution secondary-eclipse emergent spectrum (see Section 2.1). We pass this spectrum through our observational simulator (see Section 2.3) to generate the data points with associated uncertainties at a particular resolution, assuming we have used *Spitzer*, *HST*, and *JWST* observations (Greene *et al.* 2016). Using the Bayesian Atmospheric Radiative Transfer code, BART (see Section 2.2), we then run retrievals on different combinations of data sets and explore the resulting posterior distributions of model parameters to assess how well the observations discriminate between different physical and chemical models (Blecic 2016, Cubillos 2016, Chapters 5). Comparing our retrieved temperature structure with our 3D inputs, we are particularly interested in which temperature profile is revealed by the retrieval. Conclusions reached in this analysis are independent of the validity of the detailed solution provided by the hydrodynamic solution. Our goal was to investigate how well a set of temperature–pressure

profiles describing a 3D structure of an object can be retrieved with the 1D retrieval approach. In this paper, we exclude clouds and hazes from the analysis.

We used the existing numerical tools that have been well tested in the literature (Dobbs-Dixon & Agol 2013, Blecic 2016, Blecic *et al.* 2016, Greene *et al.* 2016) and developed several new ones to perform the 3D–1D comparison. All of the tools are open-source software available to the community under the RR license (see Section 6). Below, we describe each of them and give webpage links where they can be found. Additional information on the algorithms can be found in the referenced papers.

### 2.1. RHD

RHD is a 3D radiative-hydrodynamic atmospheric simulator (Dobbs-Dixon & Agol 2013). The code solves the fully comprehensive Navier-Stokes equations coupled with the wavelength-dependent radiative transfer to assess the hydrodynamics and radiative capacity of the entire planet envelope. The equations are solved in spherical coordinates with the resolution  $(N_r, N_\phi, N_\theta) = (100, 160, 64)$ , where  $r$  is the radial distance,  $\phi$  is the longitude, and  $\theta$  is the latitude. Transfer of energy via radiation employs a frequency-dependent two-stream approximation (Mihalas *et al.* 1978). The full planetary spectrum is divided into 30 bins using averaged frequency-dependent opacities from Sharp & Burrows (2007). The code considers absorption due to the four main and most spectroscopically active species in hot Jupiters,  $\text{H}_2\text{O}$ ,  $\text{CO}$ ,  $\text{CO}_2$ , and  $\text{CH}_4$ . To mimic the effect of clouds, an additional opacity is added, consisting of both a gray and a Rayleigh scattering component. There has been some criticism (e.g., Amundsen *et al.* 2014, 2016) that this simplified averaged approach to radiative transfer will yield erroneous thermal profiles when compared to more sophisticated techniques used by other groups (Showman *et al.* 2009). However, Dobbs-Dixon & Agol (2013) undertook a detailed comparison between the simulations and available observations, showing that the results compared favorably for transit, emission, and phase curve observations, suggesting that the calculated thermal profiles are sufficiently adequate for our purposes here. More on the radiative-hydrodynamic solution of HD 189733b can be found in Dobbs-Dixon & Agol (2013). The output of this code used in this analysis can be found on [github.com/dzesmin/RRC-BlecicEtal-2017-ApJ-3Dretriev](https://github.com/dzesmin/RRC-BlecicEtal-2017-ApJ-3Dretriev).

### 2.2. BART

BART (Blecic 2016, Cubillos 2016, Chapters 5), initializes a model for the atmospheric retrieval calculation, generates thousands of theoretical model spectra using parametrized pressure and temperature profiles and line-by-line radiative transfer calculations, and employs a statistical package to compare the models with the observations (Blecic *et al.* 2017, Cubillos *et al.* 2017a, Harrington *et al.* 2017, in prep.). Given transit or eclipse observations at multiple wavelengths, BART retrieves the thermal profile and chemical abundances of the selected atmospheric species. It initializes a model atmosphere using the Thermochemical Equilibrium Abundances (TEA) code (Blecic *et al.* 2016) or a vertically uniform abundances-profile routine, calculates model spectra using a radiative-transfer routine, Transit (Rojo 2006), and is driven through the parameter space using the Multi-core Markov-chain Monte Carlo statistical algorithm (Cubillos *et al.* 2017b).

Transit’s emission spectra models agree with models from Caroline Morley within a few percent (see Figures 5.5 and 5.6 in Cubillos 2016, Chapter 5). Our opacity spectra are consistent with those from Sharp & Burrows (2007) (see Figure 5.7 in Cubillos 2016, Chapter 5). To perform a retrieval validation test, we applied BART to synthetic observations of a hot-Jupiter planet with the characteristics of the HD 209458 system (see Figure 5.8 in Cubillos 2016, Chapter 5). The best-fitting model and the posterior distributions of the temperature profile and abundances agree within the  $1\sigma$  credible region of the input values.

BART was applied to *Spitzer*, *HST* and ground-based eclipse observations of the hot-Jupiter planet WASP-43b (Section 5.4 in Blečić 2016, Chapter 5) and to the *Spitzer* and *HST* transit observations of the Neptune-sized planet HAT-P-11b (Section 5.4 in Cubillos 2016, Chapter 5). For the analysis of WASP-43b, our models confirmed a decreasing temperature with pressure, a solar water abundance and a mildly enhanced C/O ratio consistent with previous analyses (Line et al. 2013, Blečić et al. 2014, Kataria et al. 2015, Benneke 2015). For HAT-P-11b, we reproduced the conclusions of Fraine et al. (2014) by constraining the H<sub>2</sub>O abundance and finding an atmosphere enhanced in heavy elements.

In the following sections, we give more details about each of the independently working routines of BART. BART is written in Python and C, and is available to the community under an open-source RR license via <https://github.com/exosports/BART>.

### 2.2.1. TEA

TEA (Blečić et al. 2016) calculates the mixing fractions of gaseous molecular species following the method by White et al. (1958) and Eriksson (1971). Given a  $T$ - $P$  profile and elemental abundances, TEA determines the species abundances by minimizing the total Gibbs free energy of the system, using an iterative Lagrangian steepest-descent method that minimizes a multivariate function under constraint. To guarantee physically plausible positive mixing fractions, TEA implements the lambda correction algorithm. TEA is tested against the analytical models developed by Burrows & Sharp (1999), Heng & Tsai (2016), and the free thermochemical equilibrium code Chemical Equilibrium with Applications (CEA, <http://www.grc.nasa.gov/WWW/CEAWeb/>, Gordon & McBride 1994). The code is open-source and available to the community under the RR license at <https://github.com/dzesmin/TEA>.

### 2.2.2. Transit

Transit is a 1D line-by-line radiative-transfer code originally developed at Cornell University by Patricio Rojo and further modified at the University of Central Florida (Blečić 2016, Cubillos 2016, Chapters 5). The code can produce both transmission and hemisphere-integrated emission spectra assuming hydrostatic balance, local thermodynamic equilibrium, and an ideal gas law. The opacities come from the HITRAN/HITEMP database, <https://www.cfa.harvard.edu/hitran>, where the line transitions are due to electronic, rotational, and vibrational absorptions and collision-induced absorption (CIA). The partition functions for the HITRAN opacity sources were calculated based on Laraia et al. (2011). The CIA data come from Borysow et al. (2001), Borysow (2002) and Richard et al. (2012). Transit takes an atmospheric model, line-list database, CIA, and

molecular information and calculates how the ray is traveling through the planetary atmosphere for the desired geometry and wavelength range.

Transit performs a line-by-line opacity calculation by applying a dynamical wavenumber sampling routine. The routine finds a minimum width of the lines at every atmospheric layer to avoid undersampling of narrow line profiles and oversampling of wide line profiles (which would significantly slow down the line-by-line computation). The resolution is then tuned down for the output spectrum to a user-desired value (see the Transit User Manual at <https://github.com/exosports/transit/>). To speed up the spectrum calculation, Transit provides an option to precalculate the opacity grid and interpolate the opacities from the table.

The Transit code was used to detect water in the atmosphere of the extrasolar planet HD 209458b using transit spectroscopy (Rojo 2006, Rojo et al. 2009). The code is available to the community under the RR license at <https://github.com/exosports/transit>.

### 2.2.3. McCubed

To explore the phase space of thermal profiles and species abundances parameters, BART uses the Multi-core Markov-chain Monte Carlo module (McCubed, Cubillos 2016). McCubed is an open-source fitting tool that uses Bayesian statistics to estimate the best-fitting values and the credible regions for the model parameters. It provides three routines to sample the parameter posterior distributions: Differential-Evolution (DEMC, Braak 2006), Metropolis Random Walk (using multivariate Gaussian proposals), or the Snooker-updater DEMC algorithms (ter Braak & Vrugt 2008). The DEMC routine, in particular, significantly improves the MCMC efficiency. By computing the proposed jump for a given chain from the difference between the parameter states of two other randomly selected chains, as the chains approach convergence (Gelman & Rubin 1992), DEMC adjusts the scale and orients it along the desired distribution. McCubed is used in the correlated-noise analyses applied to the exoplanet light curves by Cubillos et al. (2017b). The code is written in Python using several C-routines and is documented and available to the community via <https://github.com/pcubillos/McCubed>.

## 2.3. Observation Simulation Tool

We developed a code to simulate observations of theoretical emission spectra following Greene et al. (2016). In addition to the *JWST* (NIRISS, NIRCAM/NIRSpec, and MIRI LRS) simulated observations described in Greene et al. (2016), we extended this code to simulate *HST* (WFC3 G141) and *Spitzer* (IRAC Channel 1 and 2) observations of modeled planets and their host stars. This code computes the signal in electrons expected to be collected over a given period, accounting for all observatory wavelength-dependent throughputs as well as the duty cycle set by the readout options without saturation in each instrument mode. System throughputs were obtained from the *JWST* instrument teams or the STScI website (when available), the [www.ipac.caltech.edu](http://www.ipac.caltech.edu) website (*Spitzer* IRAC channels 1 and 2), and the *HST* WFC3 documentation on the STScI website. Noise from photo-electron Poisson statistics, detector readouts, detector dark currents, and observatory backgrounds was also included. A noise floor was also added to approximate the best results achieved in the transit community literature or expected (*JWST*) for each mode (20 ppm for *HST* G141 and *JWST* NIRISS, 30 ppm for *Spitzer* IRAC

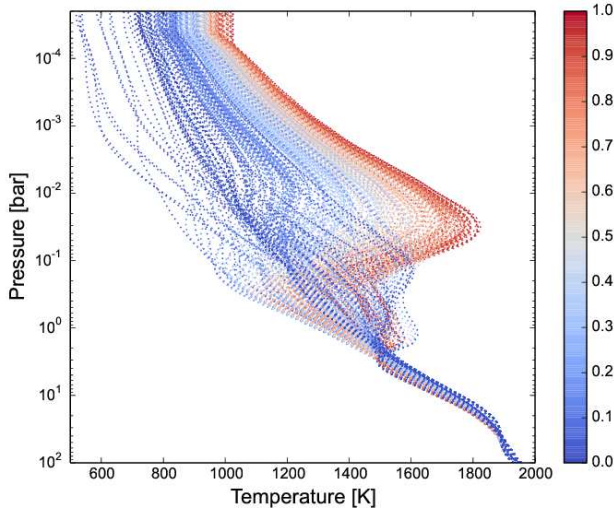


FIG. 1.—  $T$ - $P$  profiles of the HD 189733b dayside sampled on every 10 degrees latitude and longitude, generated using RHD. The color bar shows  $\mu = \cos(\text{long}) * \cos(\text{lat})$ , with  $\mu = 1.0$  (red) at substellar point, and  $\mu = 0.0$  (blue) at terminator.

channels 1, 2 and *JWST* NIRC*am*, and 50 ppm for *JWST* MIRI LRS). These noise terms were combined in quadrature to estimate the  $1\sigma$  uncertainties in each spectral bin.

### 3. THEORETICAL MODEL

To start our analysis, we take one snapshot from the radiative-hydrodynamic simulation of HD 189733b (when the upper atmosphere,  $p \lesssim 10$  bars, of the simulation has reached a steady state) and process the 3D temperature and pressure structure. The thermal structure of HD 189733b is strongly affected by the presence of supersonic winds that efficiently advect the energy from the day- to the nightside of the planet. The super-rotational equatorial jet is present between  $10^{-5}$  to 10 bars, and counter-rotational jets are present at the higher latitudes.

The 3D temperature and pressure structure obtained from the radiative-hydrodynamic solution is then interpolated on a constant pressure grid (constrained between  $2 \times 10^{-5}$  and  $10^2$  bars and sampled 100 times uniformly in log space), and the temperature profiles are extracted on every 10 degrees longitude and latitude along the dayside of the planet. Figure 1 shows the ensemble of temperature and pressure profiles from the dayside atmosphere of HD 189733b that was used in the analysis.

Utilizing TEA, we then used these temperature–pressure profiles to calculate chemical species abundances. Assuming the solar elemental composition from Asplund *et al.* (2009), TEA included H, He, C, N, and O elemental species and the following molecular species:  $\text{H}_2$ , CO,  $\text{CO}_2$ ,  $\text{CH}_4$ ,  $\text{H}_2\text{O}$ ,  $\text{N}_2$ , HCN,  $\text{NH}_3$ ,  $\text{C}_2\text{H}_2$ , and  $\text{C}_2\text{H}_4$ . The mixing ratios of all included species are calculated at each 3D location on the dayside hemisphere of HD189733.

To produce planetary intensities at every location on the planet surface, we used the Transit radiative-transfer code together with the results from TEA and the line-by-line opacity data. We employed the HITRAN and HITEMP databases to include the influence of the line-list data. We choose four main molecular species,  $\text{H}_2\text{O}$ , CO,  $\text{CO}_2$ , and  $\text{CH}_4$ , as they have the most significant spectral features on the wavelength

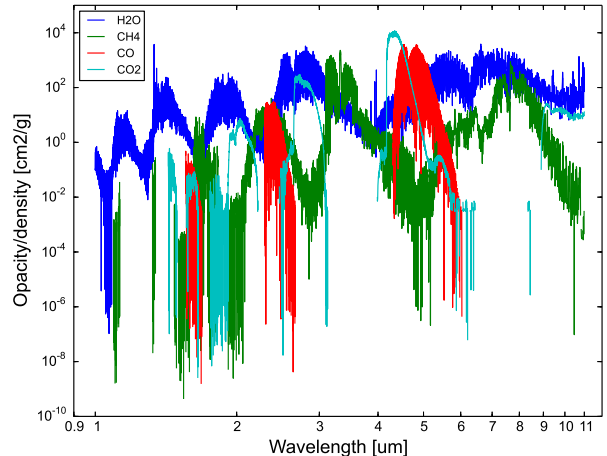


FIG. 2.— Opacities of the four main molecular species ( $\text{H}_2\text{O}$ , CO,  $\text{CO}_2$ , and  $\text{CH}_4$ ) used in our analysis, calculated at a temperature of 1500 K and a pressure of 1 bar. The gaps in the opacity curves come from the limited y-axis range (the values not shown are well below  $10^{-12} \text{ cm}^2 \text{ g}^{-1}$ ). The line lists come from the HITRAN or HITEMP databases.

range of our interest (Figure 2). For  $\text{H}_2\text{O}$ , CO, and  $\text{CO}_2$ , we used the HITEMP database, Rothman *et al.* (2010) and for  $\text{CH}_4$ , we used Rothman *et al.* (2013). The CIA opacities for  $\text{H}_2$ - $\text{H}_2$  and  $\text{H}_2$ -He came from Richard *et al.* (2012).

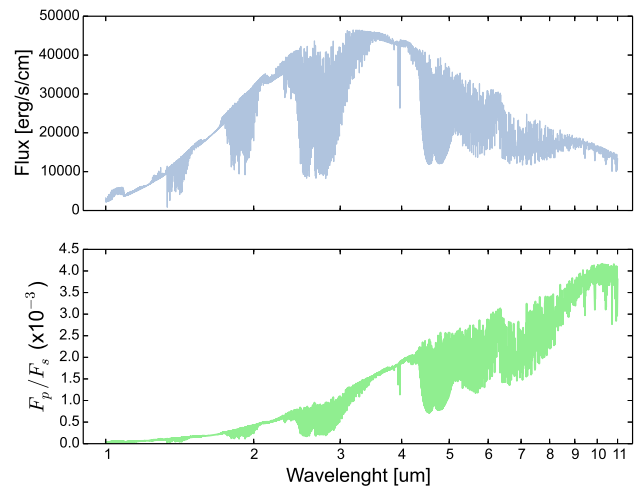


FIG. 3.— Top: the HD 189733b planetary model spectra (flux) produced using the 3D  $T$ - $P$  profiles from Figure 1. TEA was used to calculate species abundances, and Transit with HITRAN opacities was used to produce the spectra. Bottom: the high-resolution model spectrum (flux ratio) produced using the planetary model spectrum from the top panel and the Kurucz stellar model chosen based on the system parameters from Table 1. These spectra are henceforth treated as a real high-resolution observation

The planetary flux at the observer’s location is calculated by integrating the intensities at each location accounting for the observer’s angle. The top panel in Figure 3 shows the calculated dayside flux from the planet. The high-resolution emergent model, flux ratio, shown in the bottom panel of Fig-

TABLE 1  
SYSTEM PARAMETER VALUES

Parameter	Value	Source
$R_p(R_J)$	1.178	Triaud et al. (2009)
$M_p(M_J)$	1.138	Triaud et al. (2009)
$\log g_p$ (cgs)	2.03	Calculated
$R_*(R_{Sun})$	0.766	Triaud et al. (2009)
$M_*(M_{Sun})$	0.840	Southworth (2010)
$T_*$ (K)	5050	Bouchy et al. (2005)
$\log g_*$ (cgs)	4.610	Southworth (2010)
Fe/H	-0.03	Triaud et al. (2009)
$a$ (au)	0.0312	Triaud et al. (2009)

ure 3 is calculated using the stellar grid models from Castelli & Kurucz (2004). We adopted the system parameters (planetary mass and radius, stellar metallicity, effective temperature, mass, radius, and gravity, and the semimajor axis) listed in Table 1. These synthetic data are then used as our high-resolution model spectrum for the subsequent observational and retrieval analyses. From this point on, we treat this spectra as a *real high-resolution observation*.

The software developed to couple the output from the RHD, TEA, and Transit, and generate the high-resolution input model for the observational tools and retrieval analysis is available at [github.com/dzesmin/RRC-BlecicEtal-2017-ApJ-3Dretriev](https://github.com/dzesmin/RRC-BlecicEtal-2017-ApJ-3Dretriev) under the open-source license.

### 3.1. 1D Validation

To assess how well a 1D representation of HD 189733b matches the spectrum of BART, we compared the output of the radiative-transfer routine from Dobbs-Dixon & Agol (2013) to the Transit output. We used the 1D substellar temperature and pressure profile from the HD 189733b hydrodynamic simulation and passed it through the RHD radiative-transfer routine to compare it to the substellar output from Transit using the same setup as described above. To calculate the emission spectra from a RHD model, Dobbs-Dixon & Agol (2013) integrated through the modeled atmosphere, calculating the net emergent flux as a function of wavelength at each location on the planet. As these spectral calculations use a snapshot from the RHD simulations, we are able to use a much higher resolution in wavelength (as opposed to the necessarily simplified radiative routine used while running concurrently with the hydrodynamics). For the current calculations, we use 5000 wavelength points logarithmically spaced between 1.0 and 11.0  $\mu m$ . Further details and associated equations can be found in Dobbs-Dixon & Agol (2013).

Transit generates a spectrum with a high resolution, using a line-by-line dynamical sampling (see Section 2.2), and tunes down the resolution for the output results to 1  $cm^{-1}$  in the wavenumber space. Between 1 and 11  $\mu m$  this generates 9091 data points. To compare outputs from Transit and RHD, we binned down the Transit resolution to the same resolution as RHD, Figure 4, showing a nice match between the two radiative-transfer routines.

### 3.2. Emission Spectrum Simulations

We produced simulated secondary-eclipse observations from the high-resolution 3D model given in Figure 3 (bottom panel) using the code described in Section 2.3. This was done for the following instruments: the *JWST* instruments NIRISS, NIRCam (or NIRSpec), and MIRI LRS; for the *HST* (WFC3

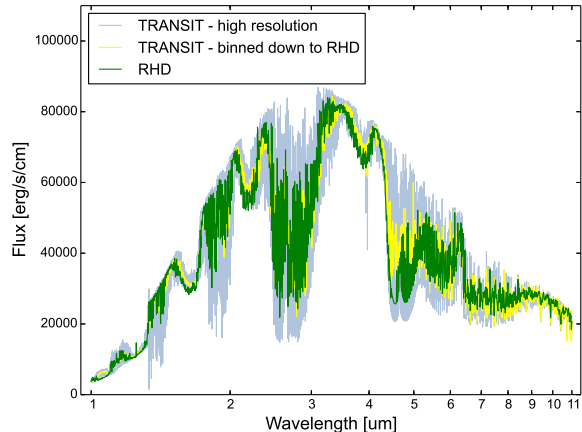


FIG. 4.— Comparison between the substellar model spectra produced using the radiative-transfer routine, Transit, and RHD. The high-resolution spectrum of Transit is shown in light blue, the Transit spectrum binned down to the RHD resolution is shown in light yellow, while the RHD spectrum is shown in green.

G141) covering the wavelength range from  $\lambda = 1.1 - 1.7 \mu m$ , and for *Spitzer* channels 1 (3.6  $\mu m$ ) and 2 (4.5  $\mu m$ ). We focus our investigation on the wavelength range between 1 and 11  $\mu m$ , as the most abundant molecular species show dominant absorption features in this region.

Several recent studies have provided an assessment of how well *JWST* will perform (Doyon et al. 2012, Beichman et al. 2014, Barstow et al. 2015, Batalha et al. 2015, Kendrew et al. 2015, Greene et al. 2016, Howe et al. 2016, Batalha & Line 2017, Mollière et al. 2017) and speculated on which modes should be used to answer certain questions. We decided to use the modes listed in Table 2 because they provide large simultaneous wavelength coverage, adequate spectral resolution, slitless operation, and bright limits sufficient to observe the HD189733 system with high throughput. Slitless spectra with good spatial sampling and stable detectors have provided the best spectrophotometric precision (Kreidberg et al. 2014). They also have the best spatial sampling available on *JWST* over their wavelength ranges; good sampling should minimize systematic errors that are due to intrapixel response variations in the presence of pointing jitter (e.g., Deming et al. 2009).

TABLE 2  
SELECTED INSTRUMENT MODES

Instrument	Mode	Optics	$\lambda(\mu m)$	Native Resolution	Sampling (Pixels)
NIRISS	bright SOSS	GR700XD	1.0 - 2.5	700	$\sim 25$
NIRCam	LW grism	F322W2	2.5 - 3.9	1400	$\sim 2$
NIRCam	LW grism	F444W	3.9 - 5.0	1550	$> 2$
MIRI	SLITLESS	LRS prism	5.0 - 11	100	$> 2$
<i>HST</i> WFC3	SLITLESS	G141	1.1 - 1.7	140	125
<i>Spitzer</i>	IRAC	Channel 1	3.2 - 3.9	0.65	$\sim 2$
<i>Spitzer</i>	IRAC	Channel 2	4.0 - 5.0	0.74	$\sim 2$

All spectra were simulated for a single 1.8 hr secondary eclipse of HD 189733b with equal time spent on the star and planet. Signal ( $F_p/F_*$ ) and  $1\sigma$  noise values are computed for each spectral resolution element of each instrument mode.

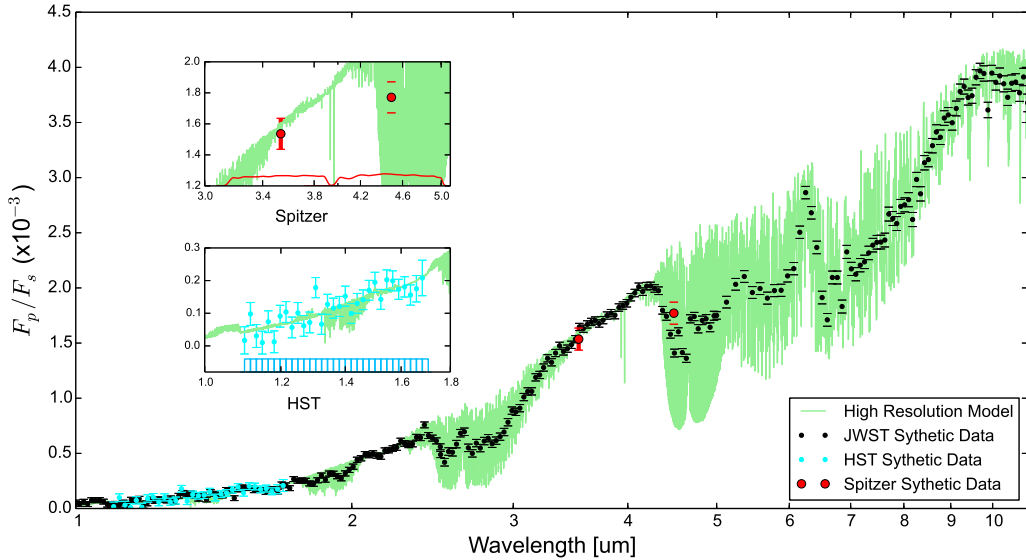


FIG. 5.— High-resolution model spectrum from Figure 3, bottom panel, with synthetic data points and uncertainties for the *JWST* (black points), *HST* (blue points), and *Spitzer* (red points), produced using the observational tools from Section 2.3. In the inset plots we zoom in on the *HST* and *Spitzer* data points and show their uncertainties along with the bandwidths of their channels/bins (2 for *Spitzer* in red, and 31 for *HST* in blue). We do not plot the bandwidths for the *JWST* in the main plot for clarity, as there are 229 tightly packed bins.

The simulated *JWST* data were binned to spectral resolving power  $R \leq 100$  (only MIRI LRS has  $R < 100$  at  $\lambda \leq 7.5\mu\text{m}$ ). Simulated *HST* WFC3 G141 data were binned to  $R = 70$ . These simulated signal and noise values were then used as inputs for the retrieval process. Figure 5 shows the 3D model spectra from all instruments together with the corresponding data points and uncertainties.

#### 4. RETRIEVAL SETUP

We performed retrieval runs with the goal to provide the observational constraints derived from the *Spitzer*, *HST* and *JWST* instruments separately and then again for different combinations of instruments. The data points and uncertainties for each of our runs come from the convolution between our high-resolution model and the observation simulation code described in Section 3.2.

The initial temperature and pressure model is chosen by running several short trial runs or by taking the  $T-P$  parameter values from the literature. The equilibrium mixing fractions of the desired molecular species are calculated using TEA, providing a realistic initial model atmosphere for our retrieval runs.

We apply two parametrization schemes to explore the shapes of the best-fit  $T-P$  profiles and compare them to our initial 3D thermal structure (see Section 4.2). Each parametrization carries a particular set of free parameters. The remaining four free parameters come from the species scaling factors that we decided to vary in our analysis:  $\text{H}_2\text{O}$ ,  $\text{CO}$ ,  $\text{CO}_2$ , and  $\text{CH}_4$ . We used flat priors on all parameters, with boundary limits set to account for all possible physically plausible solutions without constraints, to allow McCubed to explore the parameter phase space thoroughly. The temperature range is constrained between 300 and 3000 K, which corresponds to the range allowed by the HITRAN/HITEMP databases’ partition functions.

For each of our runs we use ten independent chains and

enough iterations (in the range of tens of thousands) until the Gelman and Rubin convergence test for all free parameters dropped below 1% (Gelman & Rubin 1992). The transmission response functions for the *JWST* and *HST* are top-hat functions, while the *Spitzer* response functions for the channel 1 and 2 subarray observations were taken from the *Spitzer* website, <http://irsa.ipac.caltech.edu>. The system parameters used in the analysis for the parametrized temperature model and to generate the stellar spectrum from Castelli & Kurucz (2004) are listed in Table 1.

Before presenting the results of the retrieval and compar-

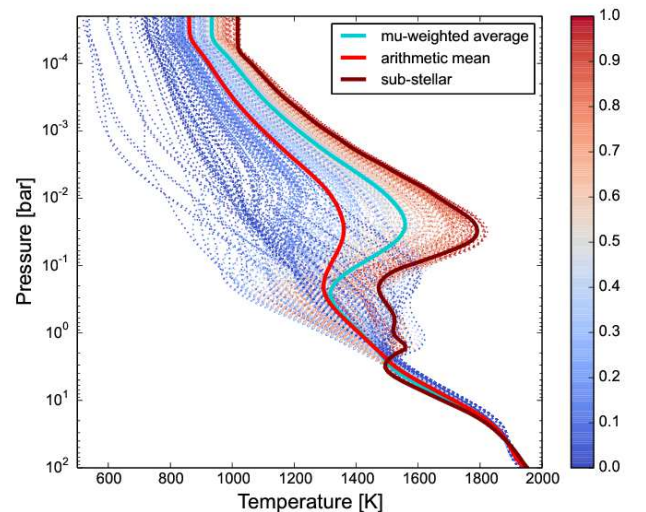


FIG. 6.—  $T-P$  profiles of the HD 189733b dayside sampled every 10 degrees in latitude and longitude, generated using RHD. The colorbar shows  $\mu = \cos(\text{long}) * \cos(\text{lat})$ , with  $\mu = 1.0$  (red) at the substellar point, and  $\mu = 0.0$  (blue) at the terminator. In turquoise color, we show the  $\mu$ -weighted  $T-P$  profile, in red the arithmetic mean, and in magenta the substellar  $T-P$  profile.

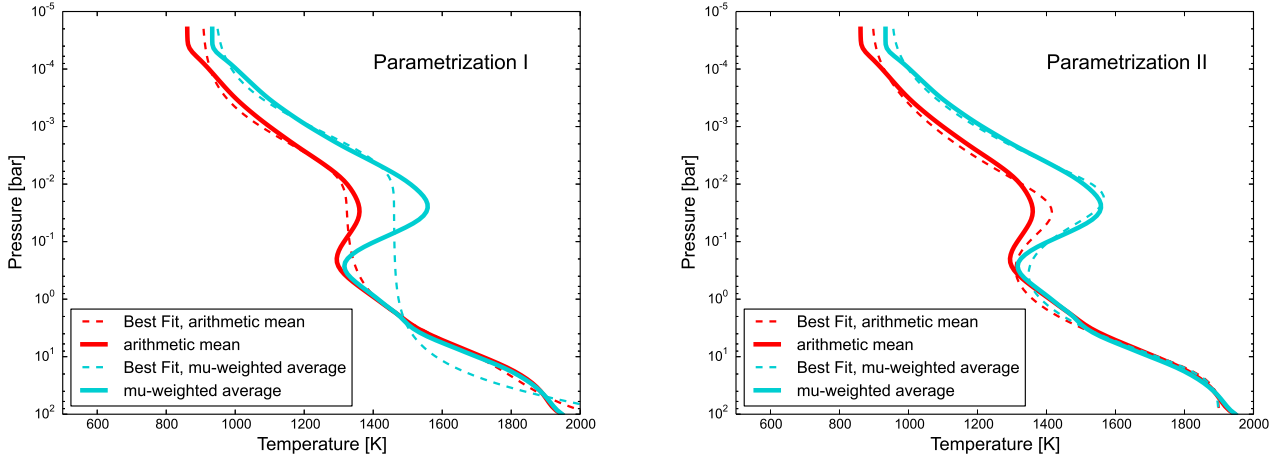


FIG. 7.— Direct fit of the  $\mu$ -weighted average and arithmetic mean  $T-P$  profiles using each of the parametrizations. Parametrization I, left panel, is unable to generate the mid-atmosphere peak seen in both the arithmetic average and the  $\mu$ -weighted average, while Parametrization II, right panel, can potentially generate this curvature.

ing them to the inputted 3D thermal structure, we apply several averages on our theoretical model to understand which average is best represented by the retrieval results. We compare these averages with the two temperature parametrizations and calculate theoretical (derived from our 3D structure) and retrieved contribution functions (derived from the best-fit retrieved models) for each of our observational instruments.

In the following sections, we explore several methods of averaging our 3D  $T-P$  profiles (Section 4.1), present the two temperature parametrization (Appendices A.1 and A.2), and discuss the way in which we calculate and average theoretical and retrieved contribution functions Sections 4.3 and 4.4.

#### 4.1. Averaging

To investigate how the retrieved  $T-P$  profile compares to the radiative-hydrodynamic model, we average the 3D day-side thermal structure of HD 189733b (Figure 1) in several ways. Considering that the emergent flux is influenced by the observer’s angle, we first calculate  $\mu$ -weighted average, where  $\mu$  is

$$\mu = \cos(\text{lat}) * \cos(\text{long}), \quad (1)$$

and the weighted average is calculated as

$$X_w = \frac{\sum_i X_i * w_i}{\sum_i w_i}, \quad (2)$$

where  $w$  is the weight. For example, if we want to average the 3D thermal structure provided by RHD, the weight is  $\mu$  and since pressure is the independent variable,  $X_i$ ’s are temperatures at each location on the dayside of HD 189733b.

We additionally consider the pure arithmetic average given by

$$X_{aver} = \frac{1}{n} \sum_{i=1}^n X_i. \quad (3)$$

Figure 6 shows all  $T-P$  profiles generated with RHD with the  $\mu$ -weighted  $T-P$  profile in turquoise, arithmetic average in red, and substellar point  $T-P$  profile in magenta.

#### 4.2. Temperature parametrization

Commonly, two temperature parametrizations are used in retrievals (Madhusudhan & Seager 2009, Line & Yung 2013). One approach is based on the parametrization described in Madhusudhan & Seager (2009) and the other has originally been developed by Guillot (2010). We have implemented both approaches to test which one produces a better match to our simulated data.

In Appendix A, we describe each parametrization in detail and explore their possible shapes, revealing the advantages and limitation of each approach. Here, we perform an optimization test, where we directly fit our averaged  $T-P$  profiles (the arithmetic average and  $\mu$ -weighted average) with both parameterizations, looking for the best fit.

To fit these profiles, we used the McCubed general fitting tool and allowed the MCMC to explore the phase space of both parametrizations until it found the best fit. We used  $5 \times 10^6$  iterations in total for each run within ten chains, and discarded the first 1000 burn-in iterations. We allowed a wide range of our parameters and started our chains in different positions of the phase space to avoid local minima.

Figure 7 summarizes the advantages and limitations of both parameterizations by showing the best-fit models to the arithmetic average and the  $\mu$ -weighted average. The left panel displays the limited capability of Parametrization I to reproduce the complex curvatures seen in these profiles. Although an inversion is possible within both of these schemes, for certain sets of parameters (see Appendix A.1, the types of inversions produced by the RHD simulations seen in Figure 6 cannot be generated. Note also that as Appendix A.1, Equation (4) gives a radiative solution, the profile must necessarily approach the isothermal solution at high pressures. The gradual steepening of the  $T-P$  profile when approaching the radiative-convective boundary cannot be captured in this model (see also Guillot 2010). However, as the radiative-convective boundary is well below the photosphere at all wavelengths, this fact does not affect the results of our retrieval.

The right panel of Figure 7 shows how well Parametrization II is able to reproduce the complex curvatures seen in both the  $\mu$ -weighted and the arithmetic averages. Using the inversion set of equations (see Appendix A.2), this approach is capable of generating the mid-atmosphere inversion peaks, as seen in

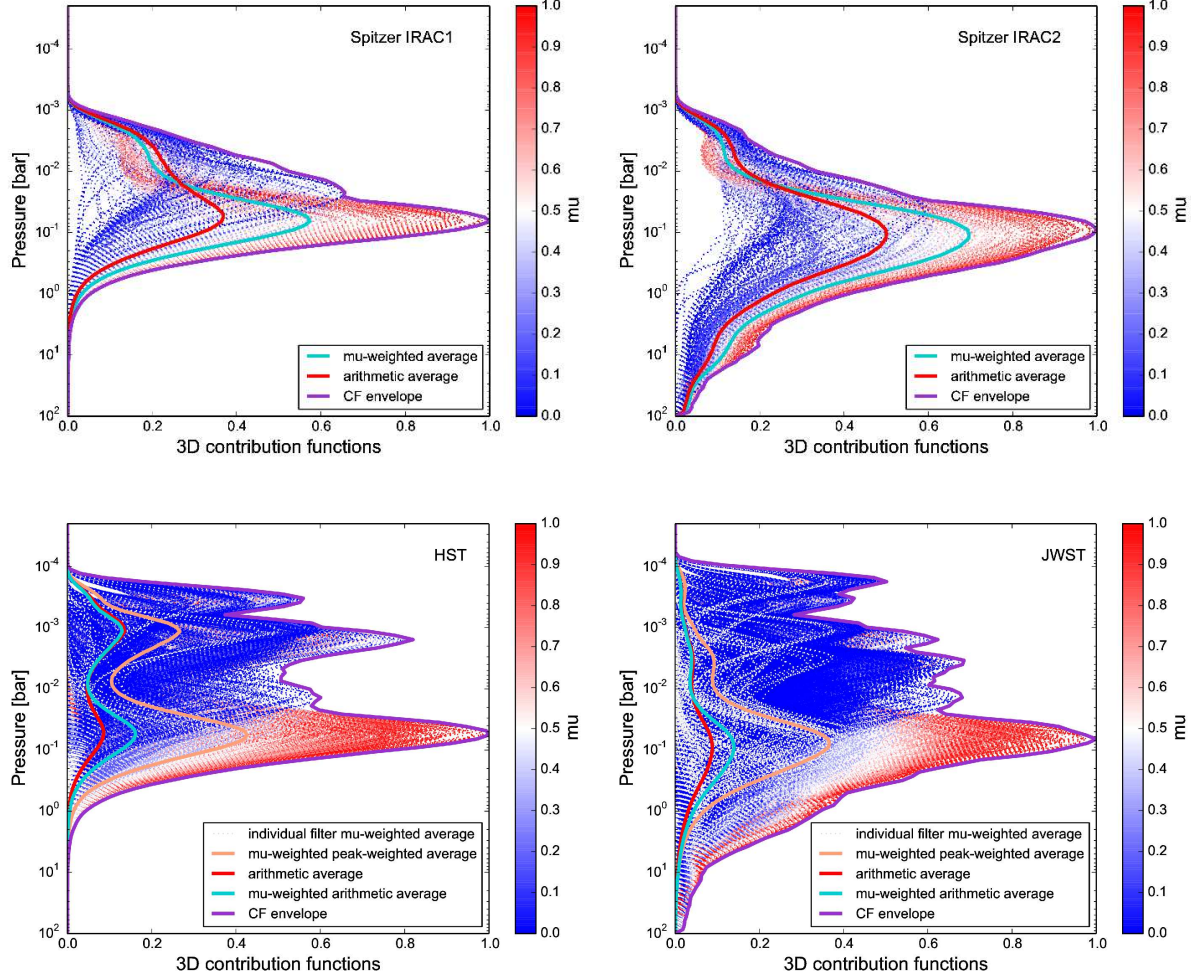


FIG. 8.— 3D theoretical contribution functions for the *JWST*, *HST*, and *Spitzer* overplotted with several averages (see Section 4.3). All contribution functions are first scaled to their maximum peak value, so their maximum value is 1. The color code is based on the observer’s angle  $\mu$ . For the *Spitzer* bandpasses, the turquoise curve is the  $\mu$ -weighted average, while the red curve is the plain arithmetic average. For the *HST* and *JWST*, we apply a pure arithmetic average for each filter and then again we use the arithmetic average between the filters (red curve). For a more realistic average, we first apply the  $\mu$ -weighted average (the white dotted curves) for each bandpass (bin), and then the overall average is calculated either by applying the plain arithmetic average between bandpasses (turquoise curve), or by applying the peak-weighted average (orange curve). To encompass the full contribution from all 3D contribution functions, we also evaluate the contribution functions envelope by calculating the maximum contribution at each pressure level.

Figure 6. The approach allows the exploration of a wide range of pressures where an inversion can occur, and can differentiate mild and strong inversions (see Appendix A.2). However, the main disadvantage of this approach is that the inversion and non-inversion cases cannot be covered with one set of equations, and each solution must be explored separately in the retrieval (Appendix A.2). This limitation forbids a statistical assessment of models produced with different numbers of free parameters.

#### 4.3. Theoretical Contribution Functions

We calculate theoretical contribution functions using our 3D thermal structure to determine which parts of the atmosphere are probed by the observations (our synthetic data points), i.e., from which pressure layers most of the flux is coming from. Our goal is to compare these theoretical contribution functions to the contribution functions from the retrieval and assess the difference, i.e. how well retrieval probes the same pressure layers as the 3D structure. To do so, we use Equation (2) from Knutson *et al.* (2009) and calculate the

contribution functions for each of the instruments separately (*JWST*, *HST*, and *Spitzer*), and investigate which part of the atmosphere would theoretically be possible to probe with each of the instruments. We calculate the contribution functions for each of the 361  $T-P$  profiles provided by our RHD simulation. In addition, to estimate where on average each instrument is probing the atmosphere of HD 189733b, we average the instrumental contribution functions in several ways (see below). Figure 8 shows the contribution functions for *Spitzer* channels 1 and 2, for the *HST*, and the *JWST*. The contribution functions are normalized to the maximum bandpass value of all contribution functions for that instrument.

The planetary emergent intensity during secondary eclipse calculated at each location (latitude and longitude) on the planet surface is influenced by the observer’s angle. The emergent flux calculated as a hemispheric average is thus strongly influenced by  $\mu = \cos(lat) * \cos(long)$ . When averaging theoretical contribution functions coming from the suite of our 3D thermal profiles (361), for each bandpass we calculate the  $\mu$ -weighted average. We also calculate the arithmetic

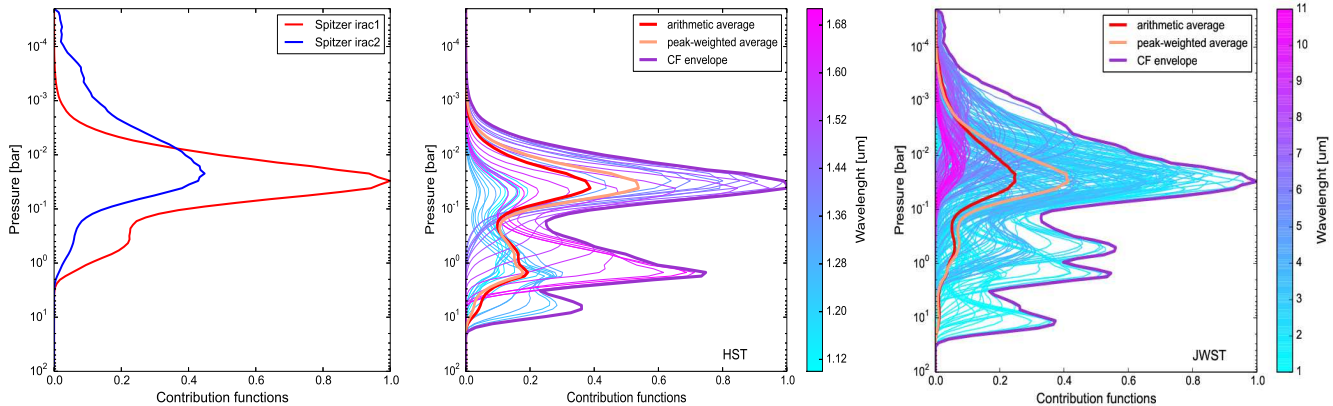


FIG. 9.— 1D retrieved contribution functions for *Spitzer*, left panel, the *HST*, middle panel, and the *JWST*, right panel, for the substellar model atmosphere. The contribution functions are overlotted with the peak-weighted contribution function (orange curve), calculated by scaling all the contribution functions to the maximum peak value, and by the plain arithmetic average (red curve). We plot the contribution function envelope in purple. The color code is wavelength based, with turquoise equal to the lower wavelength boundary and purple equal to the higher wavelength boundary for the instrument in question (*HST* in turquoise  $\lambda_{\text{low}} = 1.1 \mu\text{m}$ , and in purple  $\lambda_{\text{high}} = 1.7 \mu\text{m}$ , *JWST* in turquoise  $\lambda_{\text{low}} = 1.0 \mu\text{m}$  and in purple  $\lambda_{\text{high}} = 11 \mu\text{m}$ ). For *Spitzer* we scale IRAC channel 2 (blue) to the peak value of the IRAC channel 1 (red).

average for the sake of comparison.

*Spitzer* has two broad bandpasses, while the *JWST* and *HST* spectra both have been binned into multiple narrow bands, 229 and 31, respectively. For each filter (bandpass/bin), we calculate the  $\mu$ -weighted average and the arithmetic average as described in Section 4.1. The top two panels in Figure 8 show both the  $\mu$ -weighted and arithmetic averages for each *Spitzer* bandpass.

When we have many bandpasses (bins), we calculate the  $\mu$ -weighted averages in two different ways. Our first approach ( $\mu$ -weighted arithmetic average, turquoise lines) is to calculate the contribution functions for each  $T - P$  profile and each wavelength bandpass for each instrument. We then normalize the contribution functions to the maximum peak value of all contribution functions of that instrument. This simply scales the contribution functions to the value of 1. This approach accounts for the fact that if more flux is coming to the instrument, the signal-to-noise ratio is higher, the error bars are smaller, and this will contribute more to the result. To calculate the  $\mu$ -weighted average for each bandpass, we apply Equations (1) and (2). We then calculate the arithmetic average of the normalized contribution functions.

Our second approach to averaging ( $\mu$ -weighted peak-weighted average, orange lines) is calculated by accounting for the different contributions of each bandpass. After performing the  $\mu$ -weighted average (thin white lines), we use a peak-weighted average depending on the peak bandpass value of each contribution function.

Our third average (arithmetic average, red lines) comes from simply arithmetically averaging all 361 contribution functions of each bandpass of each instrument, and then arithmetically averaging them again based on the number of bandpasses in each instrument.

Finally, we plot the instrument contribution function envelope (*CF envelope*, purple lines) that accounts for the maximum contribution at each pressure level.

For our analysis, we use the  $\mu$ -weighted peak-weighted average and the contribution function envelope, as they seem to best represent the suite of the contribution functions.

#### 4.4. Retrieved Contribution Functions

After we retrieve the best-fit temperature profile, we calculate contribution functions for each instrument based on the best-fit model (Figure 9). Since we have only 2 bandpasses for *Spitzer*, but 31 and 229 bins for the *HST* and *JWST*, respectively, we also average the *HST* and *JWST* contribution functions to estimate where most of the flux is coming from.

We again perform two types of averaging. First, we simply scale all contribution functions for each instrument to its peak value, so that all contribution function are scaled to 1. Then, we calculate the plain arithmetic average (red curves) and the peak-weighted average (orange lines). We also plot the contribution function envelope to account for all contributions at each atmospheric layer (*CF envelope*, purple lines).

Figure 9 (middle and right panels) shows an example of how we average the contribution functions for the *HST* and *JWST*. We used the substellar model atmosphere for this example. We calculated contribution functions for each of the bandpasses/bins of each instrument. The *Spitzer* contribution functions are not averaged; instead, each bandpass contribution function was calculated separately, and two of them were scaled to their mutual maximum value (*Spitzer IRAC 1* has a higher value).

For our analysis, we use the peak-weighted average and the contribution function envelope, as they seem to best represent the suite of contribution functions for each instrument.

## 5. RESULTS

To compare the 3D temperature and pressure structure with the results from retrieval, we perform several analyses. First, we discuss the results when we only include the *JWST* synthetic points and then we discuss the results for the *HST* and *Spitzer* together, as this combination of data is often found in the exoplanetary literature. We also investigate two cases for the *JWST* analysis by using different temperature parametrization, allowing the retrieval to explore more complex thermal shapes. We first use the temperature Parametrization I, Appendix A.1, and then the temperature Parametrization II, Appendix A.2. In Appendix B, we discuss the retrieval results when we include all the synthetic data points and uncertainties for the *JWST*, *HST* and *Spitzer* together and for the *HST*

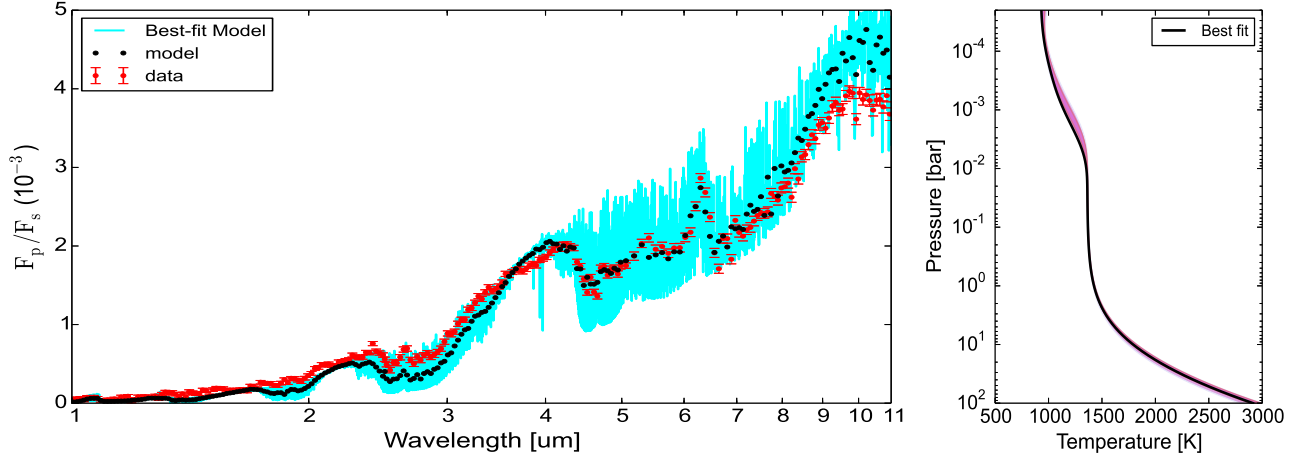


FIG. 10.— Left: The retrieved best-fit spectra (blue) for the case when *only the JWST* synthetic data are included and the temperature profile is generated using the temperature *Parametrization I*, Appendix A.1. In red are plotted the data points (eclipse depths) with error bars. In black we show the model points integrated over the bandpasses of our synthetic model. Right: the best-fit  $T-P$  profile with  $1\sigma$  and  $2\sigma$  confidence regions.

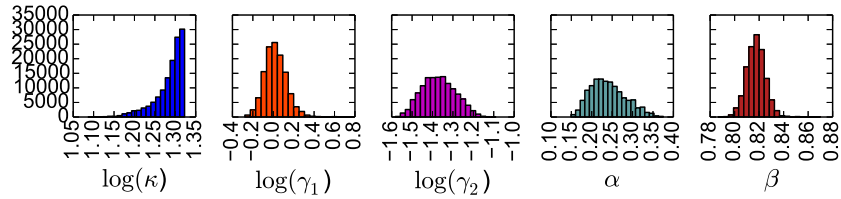


FIG. 11.— Histograms of the temperature profile parameters for the case when *only the JWST* synthetic data points are included and the temperature profile is generated using the temperature *Parametrization I*, Appendix A.1. Figures show the  $T-P$  profile parameters, where some of them are expressed as  $\log_{10}(X)$ , with  $X$  being the free parameter of the model.

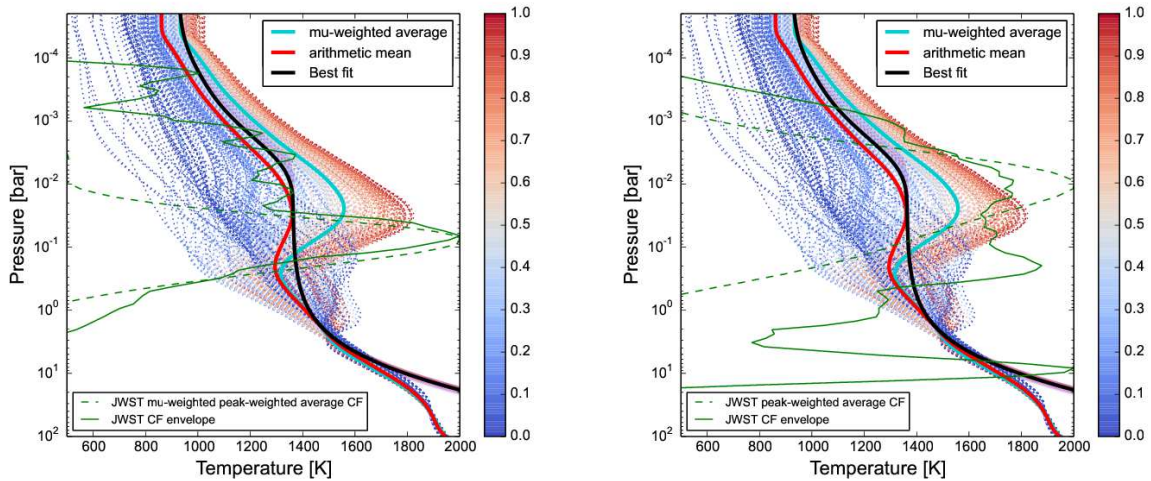


FIG. 12.— Left: the 3D  $T-P$  profile dayside structure of HD 189733b, with the retrieved best-fit temperature profile (black curve) from Figure 10, right panel, and the 3D thermal structure averages (red and turquoise curves), overplotted with *only the JWST theoretical* contribution functions, normalized to 2000, and generated using *Parametrization I*, Appendix A.1. The dotted green curve is the *JWST*  $\mu$ -weighted peak-weighted average, while the solid green curve is the *JWST* contribution function envelope (see Figure 8). Right: the 3D  $T-P$  profile dayside structure of HD 189733b, with the retrieved best-fit temperature profile (black curve) and 3D thermal structure averages (red and turquoise curves), overplotted with *only the JWST retrieved* contribution functions, normalized to 2000, and generated using *Parametrization I*, Appendix A.1. The dotted green curve is the *JWST* peak-weighted average, while the solid green curve is the *JWST* contribution function envelope.

and *Spitzer*, separately.

### 5.1. JWST

In this section, we present the results when only *JWST* synthetic data are used. We have 229 data points available, sampling the whole wavelength range between 1 and 11  $\mu\text{m}$  with

a resolution of  $\sim 100$ . First, we discuss the results when we use temperature *Parametrization I* (Appendix A.1), and then we present the results using temperature *Parametrization II* (Appendix A.2).

Figure 10 shows the best-fit spectrum and temperature profile when we use temperature *Parametrization I* with five free

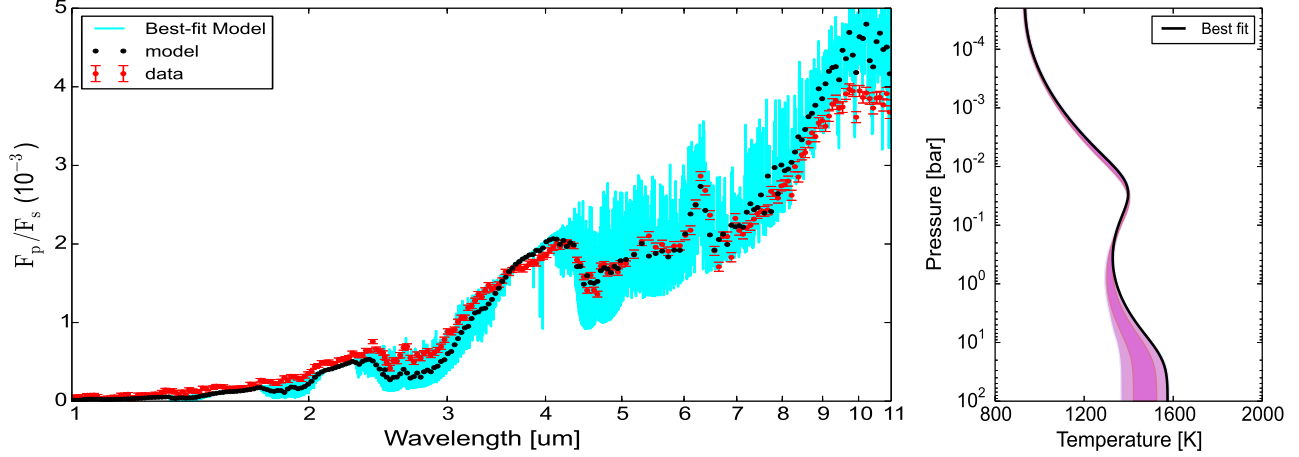


FIG. 13.— Left: the retrieved best-fit spectra (blue) for the case when *only the JWST* synthetic data are included and the temperature profile is generated using the temperature *Parametrization II*, Appendix A.2. In red are plotted the data points (eclipse depths) with error bars. In black we show are the model points integrated over the bandpasses of our synthetic model. Right: the best-fit  $T-P$  profile with  $1\sigma$  and  $2\sigma$  confidence regions.

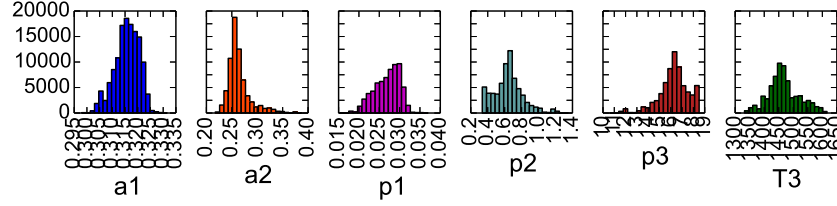


FIG. 14.— Histograms of the temperature profile parameters for the case when *only the JWST* synthetic data points are included and the temperature profile is generated using the temperature *Parametrization II*, Appendix A.2. The panels show the  $T-P$  profile parameters.

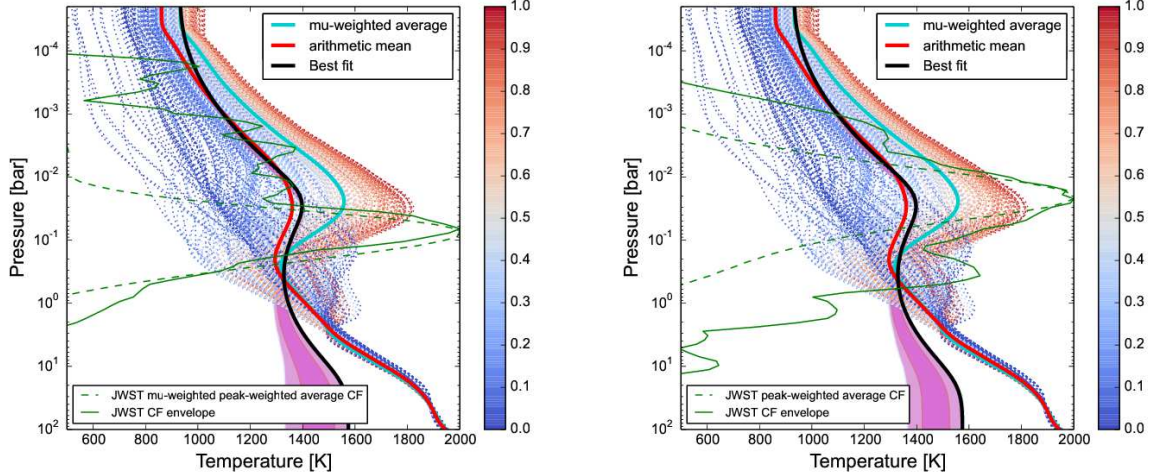


FIG. 15.— Left: the 3D  $T-P$  profile dayside structure of HD 189733b, with the retrieved best-fit temperature profile (black curve) from Figure 13, right panel, and the 3D thermal structure averages (red and turquoise curves), overplotted with *only the JWST theoretical* contribution functions, normalized to 2000, and generated using *Parametrization II*, Appendix A.2. The dotted green curve is the *JWST*  $\mu$ -weighted peak-weighted average, while the solid green curve is the *JWST* contribution function envelope (see Figure 8). Right: the 3D  $T-P$  profile dayside structure of HD 189733b, with the retrieved best-fit temperature profile (black curve) and 3D thermal structure averages (red and turquoise curves), overplotted with *only the JWST retrieved* contribution functions, normalized to 2000, and generated using *Parametrization II*, Appendix A.2. The dotted green curve is the *JWST* peak-weighted average, while the solid green curve is the *JWST* contribution function envelope.

parameters (see Appendix A.1 for possible  $T-P$  shapes using this parametrization). The spectrum and temperature structure is very similar to the case when all synthetic data (*Spitzer*, *HST*, and *JWST*) are included (see Appendix B.1). The posterior distribution (Figure 11) of the temperature parameters looks well constrained, except for the parameter  $\kappa$ . This parameter hits the wall around the same value as in the case

when all the data are included, Appendix B.1.

As shown in Appendix A.1, larger  $\kappa$  values cause the bottom of the temperature profile to go to very high temperatures, above 3000 K, which are the current boundaries for the HITRAN partition functions. Although the MCMC has a tendency to explore higher values of parameter  $\tilde{\zeta}$ , these steps are excluded from the MCMC exploration.

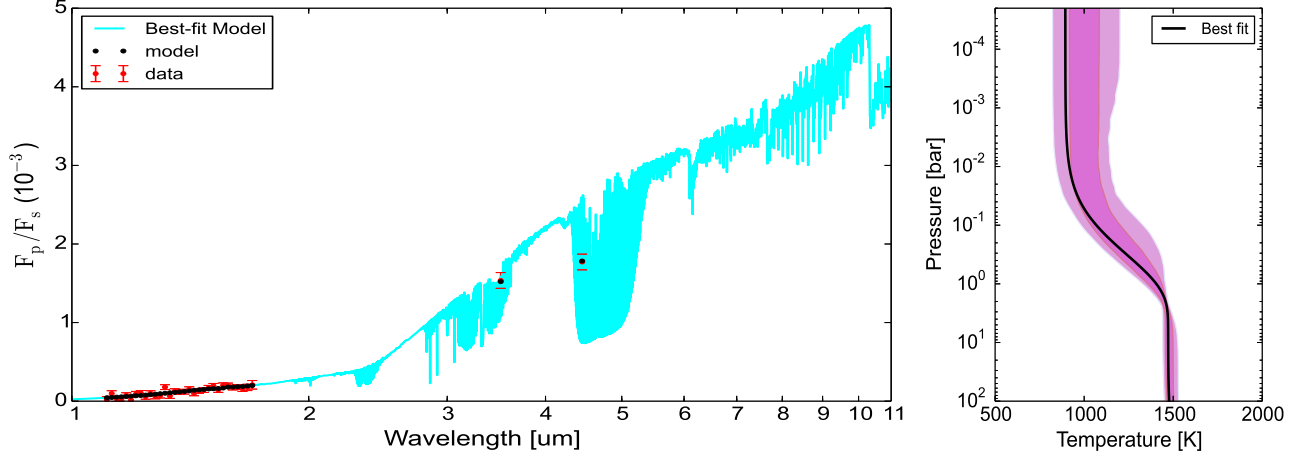


FIG. 16.— Left: the retrieved best-fit spectra (blue) for the case when *only the HST and Spitzer* synthetic data are included and the temperature profile is generated using the temperature *Parametrization I*, Appendix A.1. In red are plotted the data points (eclipse depths) with error bars. In black we show the model points integrated over the bandpasses of our synthetic model. Right: the best-fit  $T-P$  profile with  $1\sigma$  and  $2\sigma$  confidence regions.

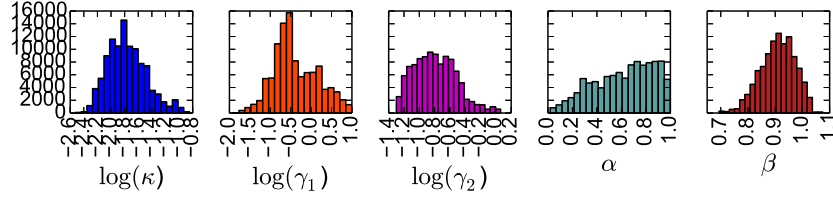


FIG. 17.— Histograms of the temperature profile parameters for the case when *only the HST and Spitzer* synthetic data points are included and the temperature profile is generated using the temperature *Parametrization I*, Appendix A.1. Figures show the  $T-P$  profile parameters, where some of them are expressed as  $\log_{10}(X)$ , with  $X$  being the free parameter of the model.

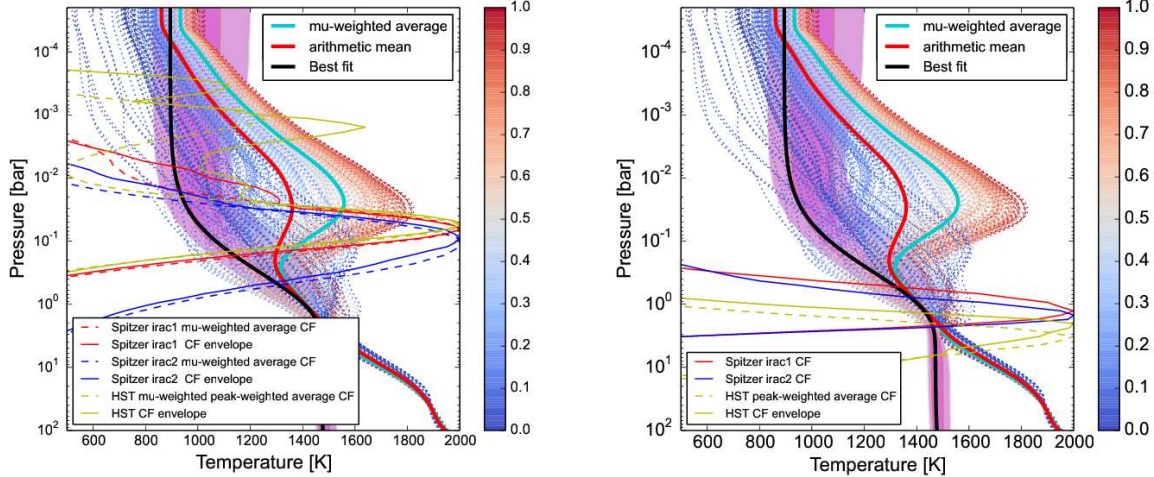


FIG. 18.— Left: the 3D  $T-P$  profile dayside structure of HD 189733b, with the retrieved best-fit temperature profile (black curve) from Figure 16, right panel, and the 3D thermal structure averages (red and turquoise curves), overplotted with *only HST and Spitzer theoretical* contribution functions, normalized to 2000, and generated using *Parametrization I*, Appendix A.1. Red and turquoise curves are *Spitzer* theoretical contribution functions, while the yellow dotted curve is the *HST* theoretical  $\mu$ -weighted peak-weighted average, and the solid yellow curve is the *HST* contribution function envelope (see Figure 8). Right: the 3D  $T-P$  profile dayside structure of HD 189733b, with the retrieved best-fit temperature profile (black curve) and 3D thermal structure averages (red and turquoise curves), overplotted with *only HST and Spitzer retrieved* contribution functions, normalized to 2000, and generated using *Parametrization I*, Appendix A.1. Red and turquoise curves are *Spitzer* contribution functions, while the yellow dotted curve is the *HST* peak-weighted average, and the solid yellow curve is the *HST* contribution function envelope.

In the left panel of Figure 12, we plot the suite of our initial 3D profiles, with both averages from Section 4.1, overplotted with the best-fit retrieved temperature profile. We also overplot the curves with the theoretical contribution functions  $\hat{\mu}$ -weighted peak-weighted average and the contribution func-

tion envelope for the *JWST*. In the right panel of Figure 12, we can see the contribution functions calculated from the retrieved best-fit model. In both cases, we plot only the averages from Sections 4.3 and 4.4 that we believe represent the best the overall contribution function trend.

As shown, both theoretical contribution functions and retrieved contribution functions sample similar pressure intervals, emphasizing that the bottom part of the temperature profile is not too reliable. The black curve does not match either the red curve (the arithmetic average) or the blue curve ( $\mu$ -weighted average), but is more similar to the red curve. Returning to Figure 7, we can see that this parametrization does not have capabilities to reproduce the complex shapes of any of these two profiles, or any of the inversion profiles seen in orange that come from the longitudes and latitudes close to the substellar point ( $0.6 < \mu < 1.0$ ).

To explore a wider range of thermal profile shapes, we run the analysis using the temperature Parametrization II (Figures 13 and 14). We see a very nice match between the best-fit model and the 3D arithmetic average (Figure 15). Although the posterior histograms in Figure 14 look somewhat worse than in the case when we had all the data included, they are still very nicely constrained. Similarly to Appendix B.1, the *JWST* contribution function of the retrieved model samples lower pressures than the theoretical contribution functions, suggesting that the most believable part of the temperature profile is actually the inversion peak.

In the literature (Knutson et al. 2007, Swain et al. 2008, Line et al. 2014, Benneke 2015) the dayside emission of HD 189733b is always presented without the presence of a thermal inversion. However, these conclusions are based on the data coming from the *HST* and or *Spitzer* observations. In the next section, we explore the best-fit model using the synthetic data for these two instruments, simultaneously.

### 5.2. *HST* and *Spitzer*

To explore how well the currently available space telescopes for exoplanetary observations can reproduce the intrinsically 3D thermal structure, we take only the *HST* and *Spitzer* data as the input for retrieval. We have two data points for the *Spitzer* observations at 3.6 and 4.5  $\mu\text{m}$ , and 31 data points for the *HST* observations between the wavelength region of 1.1 and 1.7  $\mu\text{m}$ . In this case, we use only temperature Parametrization I (Appendix A.1) to explore the shapes of the temperature profiles, as the data lead MCMC exploration to the pure non-inversion temperature profile shapes, well represented by this temperature parametrization. We have also tried Parametrization II (Appendix A.2), but the results are quite similar.

The best-fit temperature profile is fully non-inverted (Figure 16), often seen in the literature (Knutson et al. 2007, Swain et al. 2008, Dobbs-Dixon & Agol 2013, Line et al. 2014, Benneke 2015). The posterior histograms in Figure 17 are somewhat nicely constrained, but the  $1\sigma$  and  $2\sigma$  regions of the temperature profile are rather wide.

The retrieved contribution functions for the best-fit model, Figure 18, left panel, reveal that only the pressure region around 1 bar is well probed by these observations. This is at much higher pressures than the contribution functions from the theoretical model, (Figure 18, left panel) suggesting that the best-fit model is loosely constrained by the data. The number of data points and/or the wavelength coverage is not enough to lead MCMC to models similar to any of the averages of the 3D thermal structure. The retrieved temperature profile falls in the cold 3D temperature region, close to the terminator. In Appendices B.2 and B.3 we discuss the analyses done using *HST* and *Spitzer* synthetic data separately.

## 6. CONCLUSIONS

In this paper, we investigate how well the hemispherical-average temperature model retrieved by a reverse statistically robust modeling approach compares to the non-uniform 3D dayside temperature structure coming from a hydrodynamic simulation. We take the output from the 3D radiative-hydrodynamic simulation of HD 189733b and calculate the emergent spectra on the dayside atmosphere of the planet. This spectra serves as a synthetic high-resolution model that we pass through the emission spectrum simulator to generate the data points with uncertainties for the retrieval, assuming we have used *Spitzer*, *HST*, and *JWST* observations. Starting with a 1D temperature–pressure model, the retrieval framework retrieves the best-fit spectra and temperature structure. In the main body of our manuscript, we present the retrieval results when we include the synthetic data points for the *JWST* only and for the *HST* and *Spitzer* together, focusing our analysis on the combination of data most often used in the literature. In Appendix B, we discuss our findings using all the synthetic data points and uncertainties for the *JWST*, *HST*, and *Spitzer* together, as well as the results for the *HST* and *Spitzer* separately. We explore several methods of averaging our 3D  $T-P$  profiles to facilitate comparison to our retrieval results. To assess which particular 3D temperature profile matches the retrieved one, we average the initial 3D structure by performing the  $\mu$ -weighted average and the arithmetic average. We test two temperature parametrizations that are commonly used in retrieval to thoroughly explore the possible shapes of the temperature profiles and find the best match with the 3D averages in the case when we use the *JWST* synthetic data alone. To assess which part of the atmosphere would be mostly probed with the 3D structure and which part is revealed with the retrieved best-fit models, we perform a thorough exploration of theoretical contribution functions (coming from the 3D structure) and the retrieved contribution functions. We average the complex 3D contribution functions of *Spitzer*, *HST*, and *JWST* in a way similar to the original 3D thermal profiles, and in addition, we calculate the  $\mu$ -weighted and peak-weighted average of the *JWST* and *HST* contribution functions coming from different bins. We then compare the averaged theoretical and retrieved contribution functions to determine which part of the retrieved temperature profile we should trust the most.

Our results are strongly affected by the spectral resolution and the wavelength region covered by a particular instrument. When combining the data points from different instruments, our results are strongly influenced by the number of data points included in the analysis. In addition, the results are affected to some extent by the particular temperature parametrization used in retrieval. The possible shapes of the temperature profiles produced with each parametrization are slightly different, particularly in the inversion case.

As shown, when *JWST* simulated data are included in the analysis, based on both theoretical and retrieved contribution functions, most of the emergent spectra come from the regions between  $10^1$  and  $10^{-2}$  bars, sampling the middle region of the atmosphere. In addition, the extent of the best-fit  $1\sigma$  and  $2\sigma$  temperature profile confidence regions infer that pressure regions below 1 bar and above  $10^{-3}$  bars, are less well constrained. The best-fit thermal profiles infer weak thermal inversion present in the dayside atmosphere of HD 189733b, almost matching the averaged 3D temperature profile, with a better match when temperature Parametrization

II (Appendix A.2) is used. Particularly, when we use temperature Parametrization II (Appendix A.2) and we include only *JWST* synthetic data points, we see that the 3D arithmetic average closely matches the best-fit temperature profile within the pressure layers where the retrieved *JWST* contribution functions probe the atmosphere (Figure 15). This is not seen when all the data are included (see Appendix B.1). We speculate that either the additional 31 *HST* data points drag the MCMC to a different phase space, affecting (and even better constraining) the  $\text{H}_2\text{O}$  abundance at the same time (the *HST* wavelength region of 1.1 to 1.7  $\mu\text{m}$  is mostly affected by the  $\text{H}_2\text{O}$  spectral features), or that the *HST* and *Spitzer* data are not as sensitive to temperature inversions as the *JWST* data, perhaps due to their limited spectral range and resolving power. The  $\mu$ -weighted 3D average could not be closely matched (retrieved) with any analysis, although in our opinion this would be the most realistic representation of the initial 3D structure. However, both the  $\mu$ -weighted average and the arithmetic average fall within the  $1\sigma$  and  $2\sigma$  regions of the best-fit profiles, suggesting that both solutions are plausible.

When the *JWST* data are excluded from the analysis, the best-fit thermal profile confidence regions are much wider. They become even less constrained when fewer data points are included. The retrieved contribution functions do not probe the same part of the planet atmosphere as the theoretical functions, and the best-fit thermal profile is non-inverted, which does not match the shape of the averaged 3D thermal profiles. Particularly when we include both the *HST* and *Spitzer* data points, the  $\mu$ -weighted and arithmetic averages do not even fall within the  $1\sigma$  and  $2\sigma$  region of the best-fit profile. However, the retrieved contribution functions suggest that the pressure layers between 1 and 10 bars are probed with this set of observations, and both  $\mu$ -weighted and arithmetic averages closely match the best-fit profile in this part of the atmosphere.

As discussed in Dobbs-Dixon & Agol (2013), the two-stream approximation used in the RHD simulator has some limitations. The resolution required to compute an accurate temperature profile at depth using this approach far exceeds the computation capability. As the density increases with depth, the integrated optical depth becomes very large and the profile becomes independent of the numerical resolution, resulting in the isothermal temperature–pressure profile (e.g., Rauscher & Menou 2012). As this effect is purely numerical and not motivated by the physically correct isothermal plateau (e.g. Hubeny et al. 2003), the RHD code applies a diffusive scheme at optical depth greater than 2.5, allowing a non-isothermal temperature profile below  $\sim 1$  bar.

On the other hand, the two temperature parametrizations that we used in this analysis expose different limitations in different parts of the atmosphere. Temperature Parametrization I (Appendix A.1) is unable to allow the full exploration of the parameter  $\kappa$ , because of the temperature boundaries of the HITRAN database above 3000 K. It is also incapable of generating curvatures in the middle part of the atmosphere, which would be due to the presence of temperature inversion deeper in the planetary atmosphere. In contrast, temperature Parametrization II does not allow a slope in the bottom part of the atmosphere, allowing the full exploration of the parameter space and therefore a better match with the observations in the mid part of the atmosphere. However, the slope seen in the bottom part of the 3D temperature profiles coming from the RHD simulation could not be reproduced with this parametrization. These results suggest that temperature

Parametrization II (Appendix A.2) works better, but also has certain restrictions. It is capable of reproducing more curvature in the middle part of the atmosphere often seen in the outputs of the hydrodynamic simulations (often probed with observations), but it is incapable of creating a curvature in the bottom part of the atmosphere (rarely probed with the observations). Nevertheless, it is worth noting that retrieved profiles from both temperature parametrizations are close to each other in the middle part of the atmosphere, where they show only marginal difference, and that all (except in the case when we use both *HST* and *Spitzer* synthetic data) averages fall within the  $1\sigma$  and  $2\sigma$  regions of the best-fit profiles, allowing that both averages and other similar shapes are equally plausible.

The restrictions of both approaches could be overcome by introducing an additional free parameter in the middle part of the atmosphere for temperature Parametrization I (Appendix A.1) and below the 1 bar level for temperature Parametrization II (Appendix A.2). However, including a new free parameter introduces a significant computational penalty when exploring the additional phase space, with even a possibility that the new parameter could not be constrained if the data are not good enough. When we use the real or synthetic *JWST* observations, the additional free parameters could be easily justified, as the quality of data will support good constraints of the confidence regions.

In general, the results (the retrieved temperature and pressure profile) of our comprehensive retrieval analysis using different simulated data and their combinations match in the range of pressures where the retrieved contribution functions are sampling the atmosphere. The recovered temperature and pressure profile most closely matches the arithmetic average of the initial 3D thermal structure. Although the recovered  $T-P$  profiles differ significantly in the different parts of the atmosphere depending on the combination of the data used in retrieval, they agree fairly well within the parts of the atmosphere that are probed by the observations. Thus, we can say that retrieval works well to retrieve the same  $T-P$  profile regardless of which data are used. The *JWST* synthetic data provide the best match to the averaged temperature profile using the temperature Parametrization II because of its higher flexibility to cover a wider range of possible thermal profile shapes.

Although in this analysis we start from the hydrodynamic 3D model that we believe represents a realistic dayside model of the HD 189733b atmosphere, the results of this approach are valid regardless of whether we believe in the initial model. This method can be applied to any set of temperature–pressure profiles, in an attempt to test how well the 1D retrieval can match the initial 3D structure.

We have released the software written for this analysis along with all inputs and outputs under the reproducibility-research license, allowing anybody to use it and modify it. At the same time, we require that future users/developers attach the same license to their additions to this code. We wish to ensure the reproducibility of our results, and to support the efficient progress of science. The RRC for this paper, including all the packages and documentation, is available at [github.com/dzesmin/RRC-BlecicEtal-2017-ApJ-3Dretriev](https://github.com/dzesmin/RRC-BlecicEtal-2017-ApJ-3Dretriev).

We would like to thank the contributors to SciPy, NumPy, Matplotlib, and the Python Programming Language; the open-source development website GitHub.com; and other

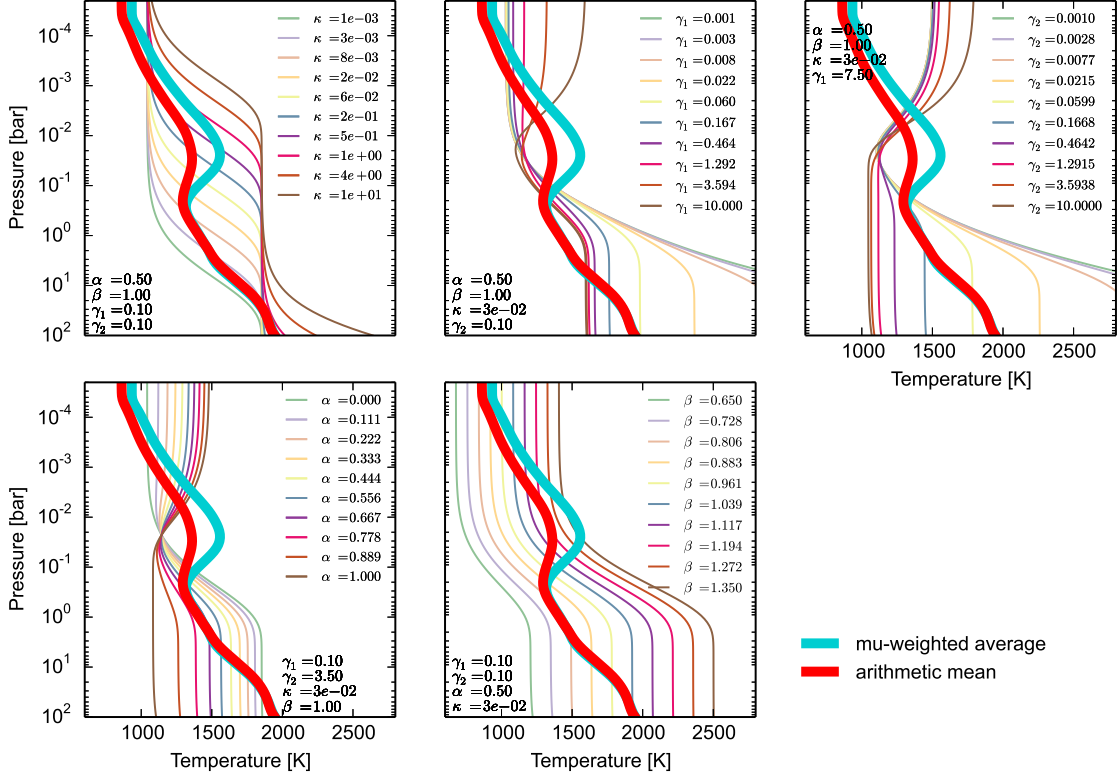


FIG. 19.— Possible temperature profile shapes generated using the temperature Parametrization I given by Equation (4), Appendix A.1. This parametrization has five free parameters,  $\kappa_{\text{IR}}$ ,  $\kappa_{v1}$ ,  $\kappa_{v2}$ ,  $\alpha$ , and  $\beta$ . In the figures  $\gamma_1 = \kappa_{v1}/\kappa_{\text{IR}}$  and  $\gamma_2 = \kappa_{v2}/\kappa_{\text{IR}}$ . In each panel, we vary different parameter and fix the remaining parameters. The profiles are overplotted with the  $\mu$ -weighted average and the arithmetic average from RHD for comparison.

contributors to the free and open-source community. J.B and I.D.D are supported by NASA through the NASA ROSES-2016/Exoplanets Research Program, grant NNX17AC03G. The research was carried out, in part, on the High Performance Computing resources at New York University, Abu Dhabi.

### A. APPENDIX

In this section we describe the two temperature parametrizations that are commonly used in retrieval. We explore their possible shapes with a goal to reveal their advantages and limitations.

#### A.1. Parametrization Scheme I

This parametrization scheme was originally formulated by Guillot (2010) and subsequently modified by Parmentier & Guillot (2014), Line & Yung (2013), and Heng et al. (2012) to include more freedom for the case when a temperature inversion is present in a planetary atmosphere. The approach is usually denoted as the three-channel approximation, where the planet temperature is given as

$$T^4(\tau) = \frac{3T_{\text{int}}^4}{4} \left( \frac{2}{3} + \tau \right) + \frac{3T_{\text{irr}}^4}{4} (1 - \alpha) \xi_{\gamma_1}(\tau) + \frac{3T_{\text{irr}}^4}{4} \alpha \xi_{\gamma_2}(\tau), \quad (4)$$

with  $\xi_{\gamma_i}$  defined as

$$\xi_{\gamma_i} = \frac{2}{3} + \frac{2}{3\gamma_i} \left[ 1 + \left( \frac{\gamma_i \tau}{2} - 1 \right) e^{-\gamma_i \tau} \right] + \frac{2\gamma_i}{3} \left( 1 - \frac{\tau^2}{2} \right) E_2(\gamma_i \tau). \quad (5)$$

$\gamma_1$  and  $\gamma_2$  are the ratios of the mean opacities in the visible to the ratio in the infrared, given as  $\gamma_1 = \kappa_{v1}/\kappa_{\text{IR}}$  and  $\gamma_2 = \kappa_{v2}/\kappa_{\text{IR}}$ . The parameter  $\alpha$  ranges between 0 and 1 and describes the relative weight of the two visible streams,  $\kappa_{v1}$  and  $\kappa_{v2}$ .  $E_2(\gamma\tau)$  is the second-order exponential integral function. The irradiation that the planet receives is given as

$$T_{\text{irr}} = \beta \left( \frac{R_*}{2a} \right)^{1/2} T_* \quad (6)$$

where  $R_*$  and  $T_*$  are the stellar radius and temperature, and  $a$  is the semimajor axis. The internal planetary flux is denoted as  $T_{\text{int}}$ . Its value is usually estimated to  $\sim 100$  K and fixed, as it has little impact on the spectra. The parameter  $\beta$  has a value of around 1 and accounts for albedo, emissivity, and day-night redistribution. The parameter  $\tau$  is the infrared optical depth calculated using the mean infrared opacity,  $\kappa_{\text{IR}}$ , pressure  $P$ , and the planet surface gravity  $g$  at one the 1 bar level:

$$\tau = \frac{\kappa_{\text{IR}} P}{g}, \quad (7)$$

Each  $T - P$  profile has five free parameters:  $\kappa_{\text{IR}}$ ,  $\kappa_{v1}$ ,  $\kappa_{v2}$ ,  $\alpha$ , and  $\beta$ . The energy balance at the top of the atmosphere is accounted for with the parameter  $\beta$ . The existence of a temperature inversion is allowed through the parameters  $\kappa_{v1}$  and  $\kappa_{v2}$ . To explore the parameter phase space, we follow Line et al. (2013), Section 3.2, when imposing boundaries.

In Figure 19, we plotted possible profile shapes using this parametrization, allowing one parameter to vary and fixing the remaining parameters. Our initial parameters are chosen to reproduce the best-fit model of the dayside atmosphere of HD

189733b from Swain *et al.* (2008). We overplotted each case with the  $\mu$ -weighted average and arithmetic averages from Figure 6.

### A.2. Parametrization Scheme II

The second temperature parametrization was originally developed by Madhusudhan & Seager (2009). In this scheme, the profiles are generated for inverted and non-inverted atmospheres separately, see Equations (11) and (12). We make minor changes to this approach as described below.

The atmosphere is divided into three layers based on the physical constraints expected in hot Jupiters, as shown in Figure 20. Layer 3, the deep isothermal layer, exists due to the strong irradiation from the parent star, which shifts the radiative-convective boundary deep in the planetary atmosphere (usually thought to be around several 100 bars). Most of the radiation is absorbed higher in the atmosphere and cannot reach the deep atmospheric layers. Layer 2, the stratospheric-radiative layer, is the zone where radiation is the dominant transport mechanism. Depending on the level of irradiation from the host star, a thermal inversion can occur. Most of the spectral features come from this layer. Layer 1, the mesospheric layer, is the layer below  $10^{-5}$  bars, important for atmospheric escape and photochemistry. This layer is transparent to the incoming and outgoing radiation in the infrared and optical, and does not affect the emergent spectra. It is heated from the lower layers and cools with increasing altitude.

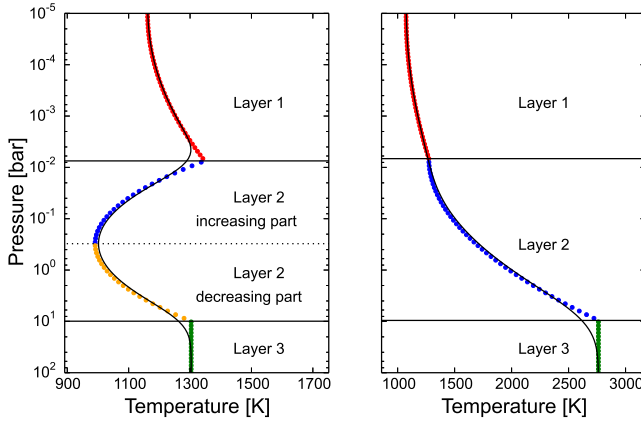


FIG. 20.— Parametric  $T$ - $P$  profiles for the inverted (left panel) and non-inverted (right panel) atmosphere based on Madhusudhan & Seager (2009). The profiles include three layers: the isothermal layer (Layer 3), the ‘stratospheric’ layer (Layer 2), the ‘mesospheric’ layer (Layer 1). Layer 2 can consist of two parts: one where temperature decreases with height, and the other where temperature increases with height, i.e., thermal inversion occurs. Different colors depict partial profiles for each layer generated using Equations (11) and (12). The dots display the number of levels in the atmosphere, which is equally spaced in log-pressure space. The thin black lines show the smoothed profile using a 1D Gaussian filter.

The following set of equations, as given by Madhusudhan & Seager (2009), describes the behavior in each atmospheric layer:

$$\begin{aligned} P_0 < P < P_1 & \quad P = P_0 e^{\alpha_1(T-T_0)^{\beta_1}} & \text{layer 1} \\ P_1 < P < P_3 & \quad P = P_2 e^{\alpha_2(T-T_2)^{\beta_2}} & \text{layer 2} \\ P > P_3 & \quad T = T_3 & \text{layer 3} \end{aligned} \quad (8)$$

This set of equations reveals 12 unknown parameters:  $P_0$ ,  $P_1$ ,  $P_2$ ,  $P_3$ ,  $T_0$ ,  $T_1$ ,  $T_2$ ,  $T_3$ ,  $\alpha_1$ ,  $\alpha_2$ ,  $\beta_1$ , and  $\beta_2$ . To decrease the number of free parameters, we made minor changes to this method. We first set  $P_0$  to the pressure at the top of the atmosphere ( $2 \times 10^{-4}$ ). The parameters  $\beta_1$  and  $\beta_2$  are empirically determined to be  $\beta_1 = \beta_2 = 0.5$  (see Madhusudhan & Seager 2009). Two of the parameters can be eliminated based on the requirement of continuity between two layer boundaries, i.e., layers 1–2 and layers 2–3. The initial guess of temperature  $T_3$  is estimated based on the equilibrium temperature of the planet. Based on the energy balance equation, the planetary equilibrium temperature is given as:

$$T_{\text{eq}}^4 = f T_{\text{eff}}^*{}^4 \left(\frac{R}{a}\right)^2 (1-A), \quad (9)$$

where the factor  $f$  describes the energy redistribution from the day- to the night side.  $f = 1/4$  defines the uniform redistribution of energy between the day- and the nightside of the planet. Since we are observing the planet dayside during secondary eclipse, we are interested in the case when none of the energy is transferred to the night side. In that case, the factor  $f$  is  $1/2$ . For a zero albedo, Equation (9) becomes

$$T_{\text{eq}}^4 = \frac{1}{2} T_{\text{eff}}^*{}^4 \left(\frac{R}{a}\right)^2. \quad (10)$$

The parametric profile for an **inverted atmosphere** has six free parameters, and these are  $P_1$ ,  $P_2$ ,  $P_3$ ,  $T_3$ ,  $\alpha_1$ , and  $\alpha_2$ . We calculate the  $T_0$ ,  $T_1$ , and  $T_2$  temperatures as

$$\begin{aligned} T_2 &= T_3 - \left(\frac{\log(P_3/P_2)}{\alpha_2}\right)^2 \\ T_0 &= T_2 - \left(\frac{\log(P_1/P_0)}{\alpha_1}\right)^2 + \left(\frac{\log(P_1/P_2)}{-\alpha_2}\right)^2 \\ T_1 &= T_0 + \left(\frac{\log(P_1/P_0)}{\alpha_1}\right)^2 \end{aligned} \quad (11)$$

For a **non-inverted atmosphere**, we assume that the Layer 2 follows an adiabatic temperature profile and exclude  $P_2$  as a free parameter. Thus, the parametric profile for the non-inverted atmosphere has five free parameters:  $P_1$ ,  $P_3$ ,  $T_3$ ,  $\alpha_1$ , and  $\alpha_2$ . We calculate  $T_0$  and  $T_1$  as

$$\begin{aligned} T_1 &= T_3 - \left(\frac{\log(P_3/P_1)}{\alpha_2}\right)^2 \\ T_0 &= T_1 - \left(\frac{\log(P_1/P_0)}{\alpha_1}\right)^2 \end{aligned} \quad (12)$$

An example of an inverted and a non-inverted profile is shown in Figure 20. To smooth the profiles so they do not have sharp kinks on the layer boundaries, we used a 1D Gaussian filter function, where 10% of total number of data points are used to smooth the data.

Figure 21 shows different profiles generated using Equation (11) by varying one parameter and fixing the rest. The top panel displays the exact solution, while the bottom panel

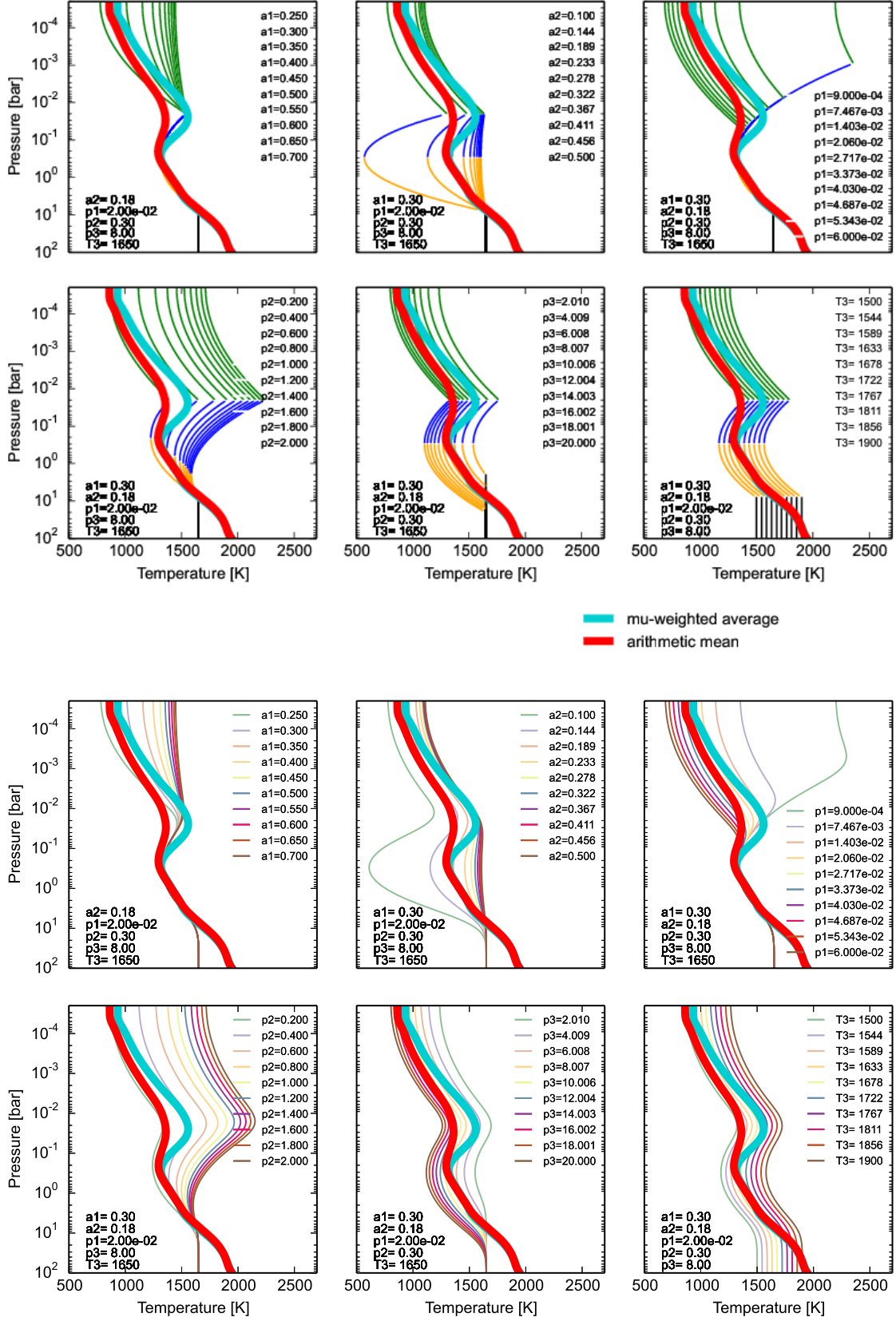


FIG. 21.— Possible temperature profile shapes generated using the temperature parametrization II given by Equation (11), Appendix A.2. This parametrization has six free parameters for the inverted atmosphere,  $P_1$ ,  $P_2$ ,  $P_3$ ,  $T_3$ ,  $\alpha_1$ , and  $\alpha_2$ . In each panel, we vary a different parameter and fix the remaining parameters. The top six panels display each layer separately, while the bottom panels show smoothed profiles. The profiles are overplotted with the  $\mu$ -weighted average and the arithmetic average from RHD for comparison.

shows smoothed profiles. We again overplot each case with the  $\mu$ -weighted average and arithmetic averages from Figure 6.

## B. APPENDIX

In this section we discuss the retrieval results when we include all three instruments together (*JWST*, *HST*, and *Spitzer*), and *HST* and *Spitzer*, separately. We test both temperature parametrizations when *JWST* data are included to investigate the more complex thermal shapes that occur in the middle region of the planetary atmosphere. The following sections elaborate on each of these cases.

### B.1. *JWST*, *HST*, and *Spitzer*

In this section we present results when all data are included. First we discuss the results when we use temperature Parametrization I (Appendix A.1) and then we present the results using the temperature Parametrization II (Appendix A.2). Figure 22 shows the best-fit spectrum and  $T-P$  profile when we use temperature Parametrization I with five free parameters (see Figure 19 for possible  $T-P$  shapes using this parametrization). Figure 23 shows the posterior histograms of the temperature profile's free parameters. As seen, all parameters except  $\kappa$  are well constrained. Parameter  $\kappa$  hits the wall around  $\log_{10}(1.3)$ , although the boundaries for this parameter are set between  $\log_{10}(-1)$  and  $\log_{10}(4)$ . As shown in Figure 19, higher  $\kappa$  values cause the bottom of the profile to extend to very high temperatures. However, the current boundaries of the HITRAN database forbid these steps. The HITRAN partition functions are not defined above temperatures of 3000 K, and these steps are excluded from the MCMC exploration. However, it is obvious that the MCMC has a tendency to explore higher values of the  $\kappa$  parameter, pushing the bottom shape of the temperature profile toward the higher temperatures, and shifting the top kink-part to lower pressures.

In the left panel of Figure 24, we plot the suite of our initial 3D profiles, with both averages from Section 4.1, overplotted with the best-fit retrieved temperature profile. We also overplot the curves with the theoretical the contribution functions  $\mu$ -weighted peak-weighted average and the contribution function envelope for each instrument. In the right panel of Figure 24, we show the contribution functions calculated from the retrieved best-fit model, again for each instrument separately. In both cases, we plot only the averages from Sections 4.3 and 4.4 that we believe represent the best the overall contribution function trend. By comparing these two panels, our goal is to show the pressure layers where each of our instruments (1) had the theoretical potential to probe the atmosphere (left panel) and (2) is actually probing the atmosphere based on the best-fit model. We also wish to see which part of the temperature–pressure profile is best represented by the data, i.e., which part of the retrieved profile we can believe.

As shown, both theoretical contribution functions and retrieved contribution functions sample similar pressure intervals, emphasizing that the bottom part of the temperature profile is not reliable. However, the black curve does not match either the red curve (the arithmetic average) or the blue curve ( $\mu$ -weighted average). Returning to Figure 19, we can see that this parametrization does not have capabilities to really reproduce the complex shapes of any of these two profiles, or any of the inversion profiles seen in orange that come from the the longitudes and latitudes close to the substellar point ( $0.6 < \mu < 1.0$ ).

The limitations of this parametrization approach led us to explore the temperatures shapes of the parametrization II, Appendix A.2. This parametrization has six free parameters for the inversion case. We set the boundaries of these parameters to account for all possible plausible scenarios and let the MCMC to explore the possible parameter space. In Figure 25 we show the best-fit spectrum and temperature profile. Figure 26 shows the posterior distribution of all six parameters. As shown, all parameters are nicely constrained. When we compare the 3D averages with our best-fit profile, we see a similar trend as in the case when we used Parametrization I (Figure 24). However, this temperature profile has more curvatures and matches the arithmetic average (red curve) somewhat better. Surprisingly, the contribution functions of the retrieved best-fit model are shifted to lower pressures compared to the theoretical contribution functions, suggesting that these observations mostly probe the pressure around  $10^{-2}$  bar (Figure 27).

### B.2. *HST*

When we only have *HST* data available, the retrieved best-fit spectrum is influenced by the synthetic data points coming from a small region between 1.1 and 1.7  $\mu\text{m}$  (Figure 28). Again, we present the results using the Parametrization I (Appendix A.1), because the results generated using Parametrization II (Appendix A.2) lead to the same conclusion.

The posterior histograms are not well constrained (Figure 29), revealing that the number of data points are not nearly enough to constrain the temperature parameters fully. The  $1\sigma$  and  $2\sigma$  temperature regions are rather wide, which allows many possible temperature scenarios. Still, the best-fit  $T-P$  profile is suggestive of a non-inverted atmosphere, again falling in the cold terminator region of our 3D temperature structure. The contribution functions for the retrieved model are well below the averaged theoretical 3D contribution functions, which prevents any conclusions about the pressure range where inversion can occur (Figure 30).

### B.3. *Spitzer*

As a final test, we use only the *Spitzer* data. Attempts have been made in the literature to make conclusions about the presence of the temperature inversion and energy redistribution (energy budget) just based on the two *Spitzer* points (e.g., Knutson *et al.* 2007, Blecic *et al.* 2013). When there is a great difference in flux values between the channels 1 and 2, and the channel 2 flux has higher brightness temperature, a thermal inversion in the planetary atmosphere is inferred.

We present here the results using temperature Parametrization I, but again we tried Parametrization II, which confirmed the same result. The spectrum looks rather flat (Figure 31), with the lines coming mostly from the region where most of the  $\text{CO}_2/\text{CO}$  and  $\text{H}_2\text{O}$  lines can be seen. The  $1\sigma$  and  $2\sigma$  regions cover a wide range of temperatures and shapes, again falling around the cold terminator region of our 3D model. The posterior histograms are not well constrained (Figure 32). The retrieved contribution functions are placed low in the planetary atmosphere, which does not provide valuable information about the inverted/non-inverted part of the atmosphere (Figure 33). However, the best-fit profile infers a non-inverted atmosphere.

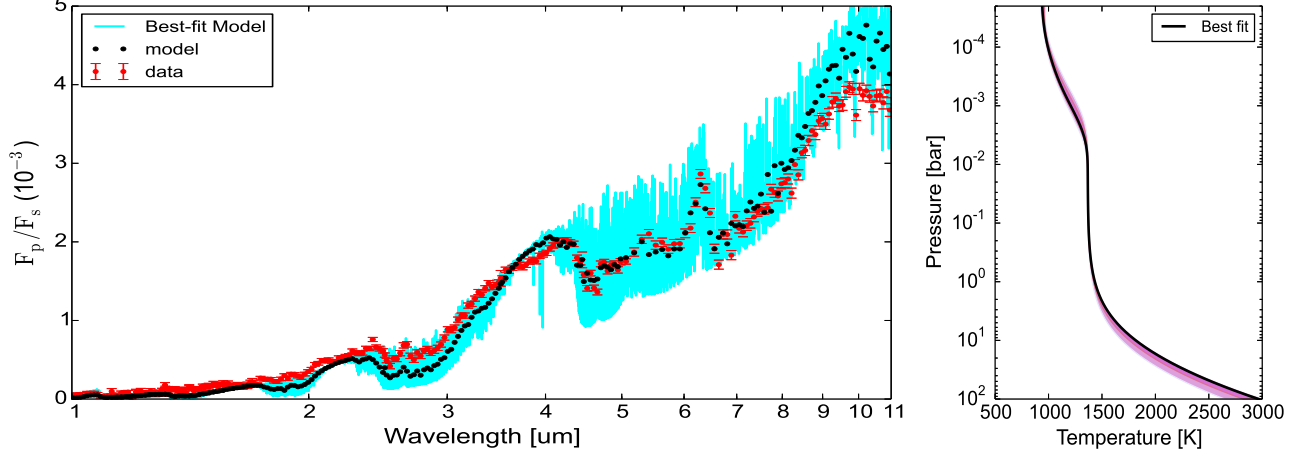


FIG. 22.— Left: the retrieved best-fit spectra (blue) for the case when *all data are included*, the JWST, HST and Spitzer and the temperature profile is generated using the temperature *Parametrization I*, Appendix A.1. In red are plotted the data points (eclipse depths) with error bars. In black we show the model points integrated over the bandpasses of our synthetic model. Right: the best-fit  $T-P$  profile with  $1\sigma$  and  $2\sigma$  confidence regions.

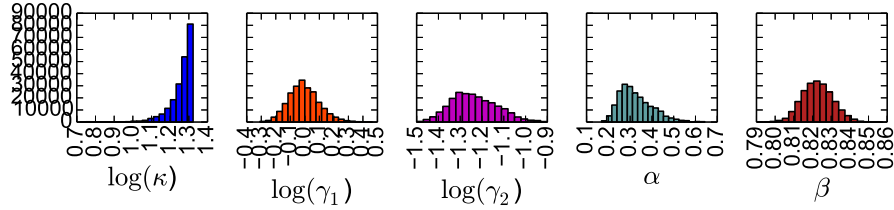


FIG. 23.— Histograms of the temperature profile parameters for the case when *the JWST, HST, and Spitzer* synthetic data points are included and the temperature profile is generated using the temperature *Parametrization I*, Appendix A.1. The panels show the  $T-P$  profile parameters, where some of them are expressed as  $\log_{10}(X)$ , with  $X$  being the free parameter of the model.

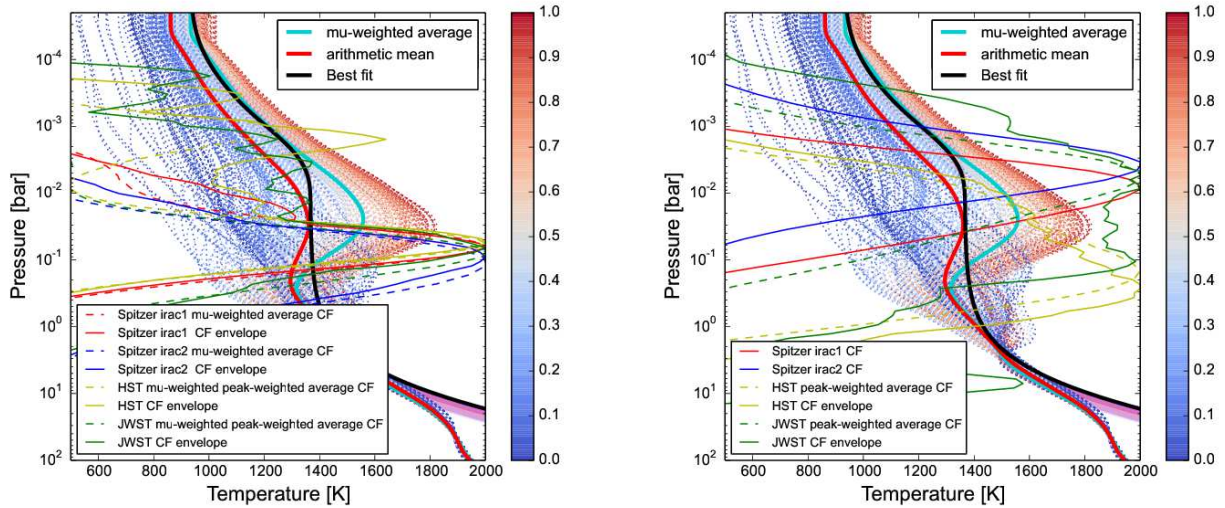


FIG. 24.— Left: the 3D  $T-P$  profile dayside structure of HD 189733b, with the retrieved best-fit temperature profile (black curve) from Figure 22, right panel, and the 3D thermal structure averages (red and turquoise curves), overplotted with *the JWST, HST, and Spitzer theoretical* contribution functions, normalized to 2000, and generated using *Parametrization I*, Appendix A.1. Red and turquoise curves are the *Spitzer* theoretical contribution functions, while the yellow dotted curve is the *HST* theoretical  $\mu$ -weighted peak-weighted average, and the solid yellow curve is the *HST* contribution function envelope. The dotted green curve is the *JWST*  $\mu$ -weighted peak-weighted average, while the solid green curve is the *JWST* contribution function envelope (see Figure 8). Right: the 3D  $T-P$  profile dayside structure of HD 189733b, with the retrieved best-fit temperature profile (black curve) and 3D thermal structure averages (red and turquoise curves), overplotted with *the JWST, HST, and Spitzer retrieved* contribution functions, normalized to 2000, and generated using *Parametrization I*, Appendix A.1. Red and turquoise curves are *Spitzer* contribution functions, while the yellow dotted curve is the *HST* peak-weighted average, and the solid yellow curve is the *HST* contribution function envelope. The dotted green curve is the *JWST* peak-weighted average, while the solid green curve is the *JWST* contribution function envelope.

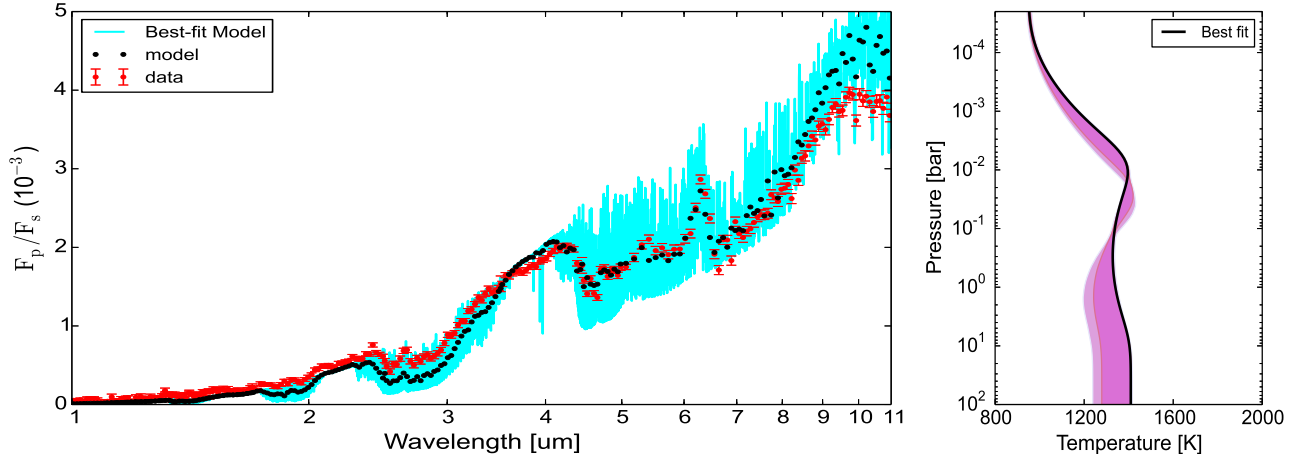


FIG. 25.— Left: the retrieved best-fit spectra (blue) for the case when *all data are included*, the JWST, HST and Spitzer and the temperature profile is generated using the temperature *Parametrization II*, Appendix A.2. In red are plotted the data points (eclipse depths) with error bars. In black we show the model points integrated over the bandpasses of our synthetic model. Right: the best-fit  $T-P$  profile with  $1\sigma$  and  $2\sigma$  confidence regions.

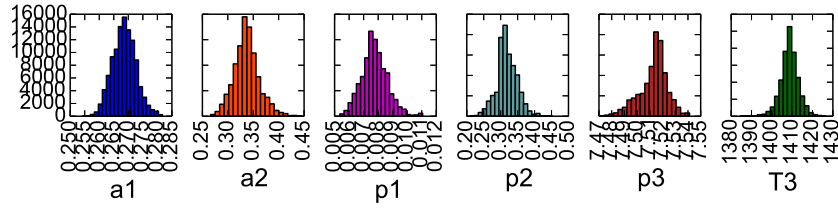


FIG. 26.— Histograms of the temperature profile parameters for the case when *the JWST, HST, and Spitzer* synthetic data points are included and the temperature profile is generated using the temperature *Parametrization II*, Appendix A.2. The panels show the  $T-P$  profile parameters.

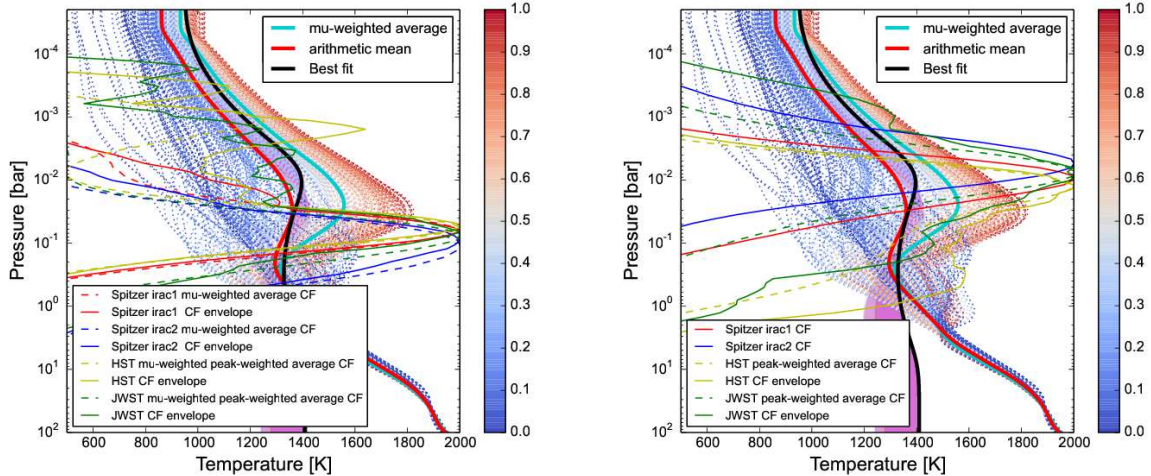


FIG. 27.— Left: the 3D  $T-P$  profile dayside structure of HD 189733b, with the retrieved best-fit temperature profile (black curve) from Figure 25, right panel, and the 3D thermal structure averages (red and turquoise curves), overplotted with *the JWST, HST, and Spitzer theoretical* contribution functions, normalized to 2000, and generated using *Parametrization II*, Appendix A.2. Red and turquoise curves are the *Spitzer* theoretical contribution functions, while the yellow dotted curve is the *HST* theoretical  $\mu$ -weighted peak-weighted average, and the solid yellow curve is the *HST* contribution function envelope. The dotted green curve is the *JWST*  $\mu$ -weighted peak-weighted average, while the solid green curve is the *JWST* contribution function envelope (see Figure 8). Right: the 3D  $T-P$  profile dayside structure of HD 189733b, with the retrieved best-fit temperature profile (black curve) and 3D thermal structure averages (red and turquoise curves), overplotted with *the JWST, HST, and Spitzer retrieved* contribution functions, normalized to 2000, and generated using *Parametrization II*, Appendix A.2. Red and turquoise curves are *Spitzer* contribution functions, while the yellow dotted curve is the *HST* peak-weighted average, and the solid yellow curve is the *HST* contribution function envelope. The dotted green curve is the *JWST* peak-weighted average, while the solid green curve is the *JWST* contribution function envelope.

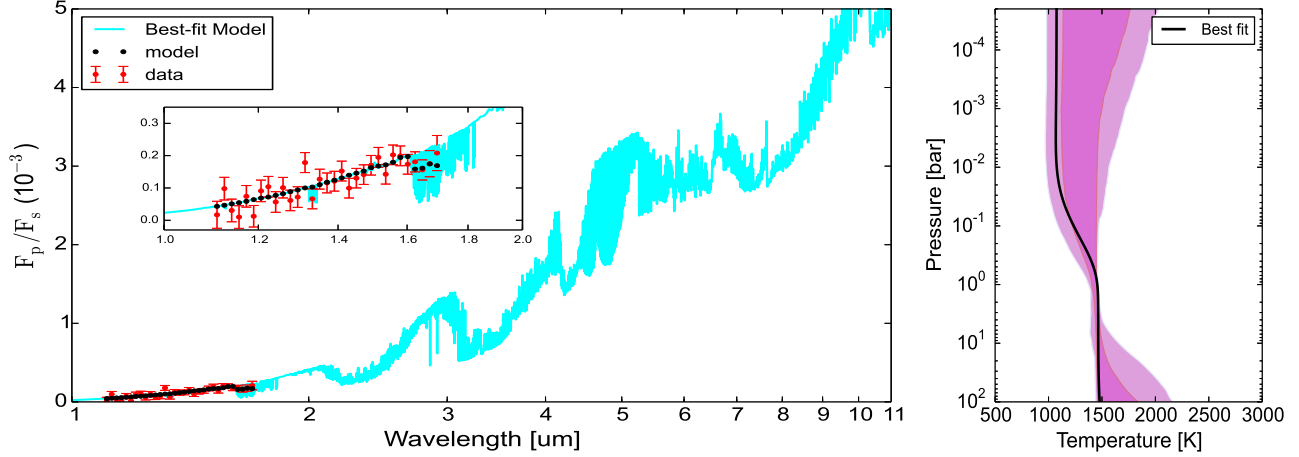


FIG. 28.— Left: the retrieved best-fit spectra (blue) for the case when *only the HST synthetic data* are included and the temperature profile is generated using the temperature *Parametrization I*, Appendix A.1. In red are plotted the data points (eclipse depths) with error bars. In black we show the model points integrated over the bandpasses of our synthetic model. Right: the best-fit  $T-P$  profile with  $1\sigma$  and  $2\sigma$  confidence regions.

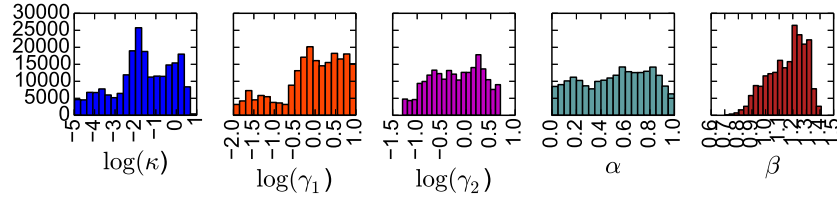


FIG. 29.— Histograms of the temperature profile parameters for the case when *only the HST synthetic data* points are included and the temperature profile is generated using the temperature *Parametrization I*, Appendix A.1. Figures show the  $T-P$  profile parameters, where some of them are expressed as  $\log_{10}(X)$ , with  $X$  being the free parameter of the model.

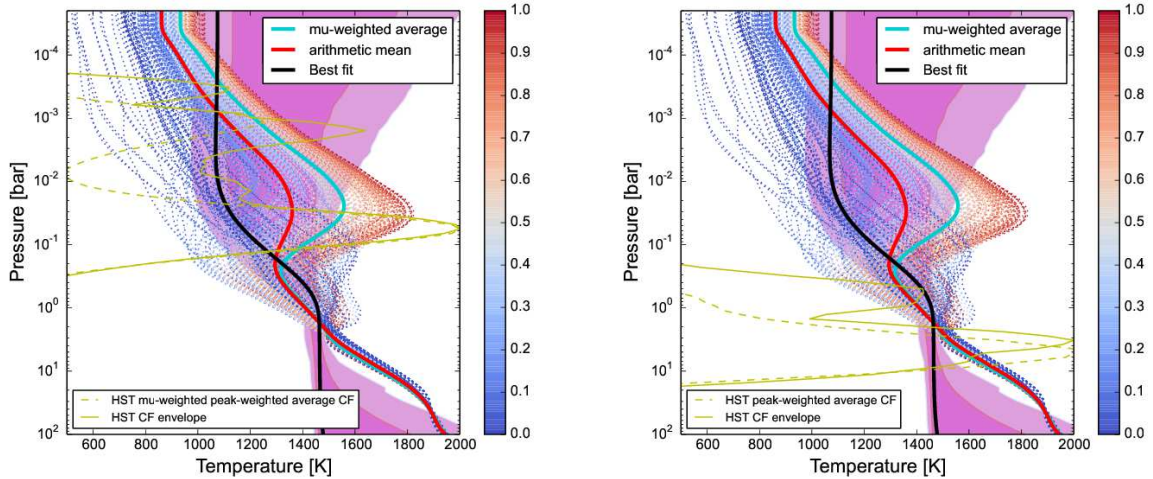


FIG. 30.— Left: the 3D  $T-P$  profile dayside structure of HD 189733b, with the retrieved best-fit temperature profile (black curve) from Figure 28, right panel, and the 3D thermal structure averages (red and turquoise curves), overplotted with *only the HST theoretical* contribution functions, normalized to 2000, and generated using *Parametrization I*, Appendix A.1. The yellow dotted curve is the *HST* theoretical  $\mu$ -weighted peak-weighted average, and the solid yellow curve is the *HST* contribution function envelope (see Figure 8). Right: the 3D  $T-P$  profile dayside structure of HD 189733b, with the retrieved best-fit temperature profile (black curve) and 3D thermal structure averages (red and turquoise curves), overplotted with *only the HST retrieved* contribution functions, normalized to 2000, and generated using *Parametrization I*, Appendix A.1. The yellow dotted curve is the *HST* peak-weighted average, and the solid yellow curve is the *HST* contribution function envelope.

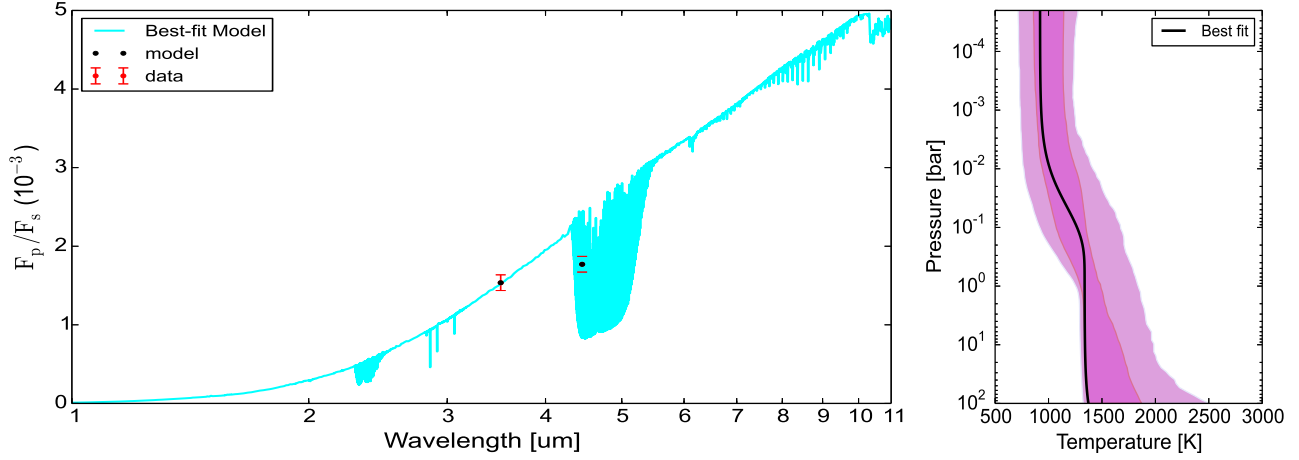


FIG. 31.— Left: the retrieved best-fit spectra (blue) for the case when *only the Spitzer* synthetic data are included and the temperature profile is generated using the temperature *Parametrization I*, Appendix A.1. In red are plotted the data points (eclipse depths) with error bars. In black we show the model points integrated over the bandpasses of our synthetic model. Right: the best-fit  $T-P$  profile with  $1\sigma$  and  $2\sigma$  confidence regions.

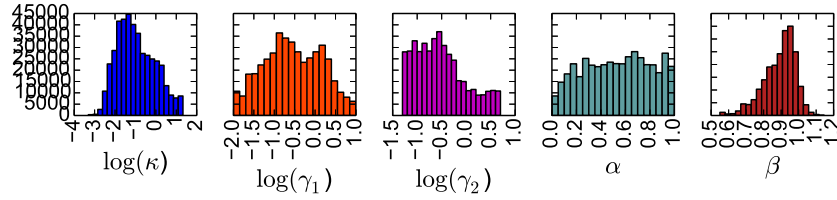


FIG. 32.— Histograms of the temperature profile parameters for the case when *only the Spitzer* synthetic data points are included and the temperature profile is generated using the temperature *Parametrization I*, Appendix A.1. The panels show the  $T-P$  profile parameters, where some of them are expressed as  $\log_{10}(X)$ , with  $X$  being the free parameter of the model.

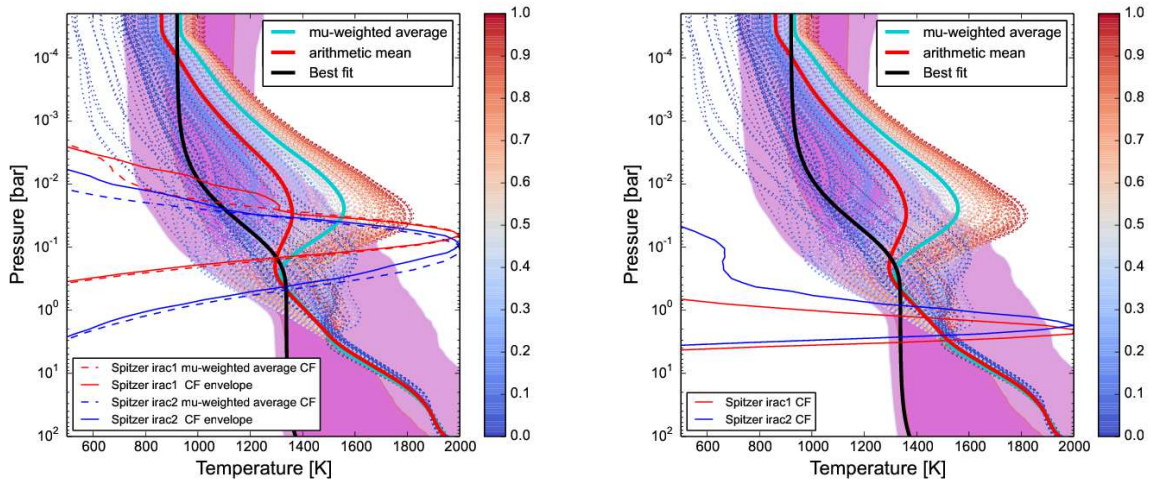


FIG. 33.— Left: the 3D  $T-P$  profile dayside structure of HD 189733b, with the retrieved best-fit temperature profile (black curve) from Figure 31, right panel, and the 3D thermal structure averages (red and turquoise curves), overplotted with *only the Spitzer theoretical* contribution functions, normalized to 2000, and generated using *Parametrization I*, Appendix A.1. Red and turquoise curves are the *Spitzer* theoretical contribution functions (see Figure 8). Right: the 3D  $T-P$  profile dayside structure of HD 189733b, with the retrieved best-fit temperature profile (black curve) and 3D thermal structure averages (red and turquoise curves), overplotted with *only the Spitzer retrieved* contribution functions, normalized to 2000, and generated using *Parametrization I*, Appendix A.1. Red and turquoise curves are the *Spitzer* contribution functions.

## REFERENCES

- Amundsen, D. S., Baraffe, I., Tremblin, P., Manners, J., Hayek, W., Mayne, N. J., & Acreman, D. M. 2014, *A&A*, 564, A59, [ADS, 1402.0814](#)
- Amundsen, D. S. et al. 2016, *A&A*, 595, A36, [ADS, 1608.08593](#)
- Asplund, M., Grevesse, N., Sauval, A. J., & Scott, P. 2009, *ARA&A*, 47, 481, [ADS, 0909.0948](#)
- Barstow, J. K., Aigrain, S., Irwin, P. G. J., Kendrew, S., & Fletcher, L. N. 2015, *MNRAS*, 451, 1306, [ADS](#)
- Batalha, N., Kalirai, J., Lunine, J., Clampin, M., & Lindler, D. 2015, *ArXiv e-prints*, [ADS, 1507.02655](#)
- Batalha, N. E., & Line, M. R. 2017, *AJ*, 153, 151, [ADS, 1612.02085](#)
- Beichman, C. et al. 2014, *PASP*, 126, 1134, [ADS](#)
- Benneke, B. 2015, *ArXiv e-prints*, [ADS, 1504.07655](#)
- Benneke, B., & Seager, S. 2012, *ApJ*, 753, 100, [ADS, 1203.4018](#)
- Blecic, J. 2016, *ArXiv e-prints*, [ADS, 1604.02692](#)
- Blecic, J., Harrington, J., & Bowman, M. O. 2016, *ApJS*, 225, 4, [ADS, 1505.06392](#)
- Blecic, J., Harrington, J., Cubillos, P., Maddison, S., & Foster, A. 2017, in prep
- Blecic, J. et al. 2014, *ApJ*, 781, 116, [ADS, 1302.7003](#)
- . 2013, *ApJ*, 779, 5, [ADS, 1111.2363](#)
- Borysow, A. 2002, *A&A*, 390, 779, [ADS](#)
- Borysow, A., Jorgensen, U. G., & Fu, Y. 2001, *J. Quant. Spec. Radiat. Transf.*, 68, 235, [ADS](#)
- Bouchy, F. et al. 2005, *A&A*, 444, L15, [ADS, astro-ph/0510119](#)
- Braak, C. J. T. 2006, *Statistics and Computing*, 16, 239
- Burrows, A., & Sharp, C. M. 1999, *ApJ*, 512, 843
- Burrows, A., Sudarsky, D., & Hubeny, I. 2006, *ApJ*, 650, 1140, [ADS, astro-ph/0607014](#)
- Burrows, A. S. 2014, *Proceedings of the National Academy of Science*, 111, 12601, [ADS, 1312.2009](#)
- Castelli, F., & Kurucz, R. 2004, *arXiv preprint astro-ph/0405087*
- Cubillos, P. et al. 2017a, in prep
- Cubillos, P., Harrington, J., Lored, T. J., Lust, N. B., Blecic, J., & Stemm, M. 2017b, *AJ*, 153, 3, [ADS, 1610.01336](#)
- Cubillos, P. E. 2016, *ArXiv e-prints*, [ADS, 1604.01320](#)
- Deming, D. et al. 2009, *PASP*, 121, 952, [ADS, 0903.4880](#)
- Dobbs-Dixon, I., & Agol, E. 2013, *MNRAS*, 435, 3159, [ADS, 1211.1709](#)
- Doyon, R. et al. 2012, in *Proc. SPIE*, Vol. 8442, *Space Telescopes and Instrumentation 2012: Optical, Infrared, and Millimeter Wave*, 84422R, [ADS](#)
- Eriksson, G. 1971, *Acta Chem.Scand.*
- Feng, Y. K., Line, M. R., Fortney, J. J., Stevenson, K. B., Bean, J., Kreidberg, L., & Parmentier, V. 2016, *ApJ*, 829, 52, [ADS, 1607.03230](#)
- Fortney, J. J., Cooper, C. S., Showman, A. P., Marley, M. S., & Freedman, R. S. 2006, *ApJ*, 652, 746, [ADS, astro-ph/0608235](#)
- Fortney, J. J., Marley, M. S., Lodders, K., Saumon, D., & Freedman, R. 2005, *ApJ*, 627, L69, [ADS](#)
- Fraine, J. et al. 2014, *Nature*, 513, 526, [ADS, 1409.8349](#)
- Gelman, A., & Rubin, D. 1992, *Statistical Science*, 7, 457
- Gordon, S., & McBride, B. J. 1994, *Computer Program for Calculation of Complex Chemical Equilibrium Compositions and Applications. I. Analysis, Reference Publication RP-1311*, NASA, describes theory and numerical algorithms behind CEA computer program
- Greene, T. P., Line, M. R., Montero, C., Fortney, J. J., Lustig-Yaeger, J., & Luther, K. 2016, *ApJ*, 817, 17, [ADS, 1511.05528](#)
- Guillot, T. 2010, *A&A*, 520, A27, [ADS, 1006.4702](#)
- Hansen, C. J., Schwartz, J. C., & Cowan, N. B. 2014, *MNRAS*, 444, 3632
- Harrington, J. et al. 2017, in prep
- Heng, K., Hayek, W., Pont, F., & Sing, D. K. 2012, *MNRAS*, 420, 20, [ADS, 1107.1390](#)
- Heng, K., & Tsai, S.-M. 2016, *ApJ*, 829, 104, [ADS, 1603.05418](#)
- Howe, A. R., Burrows, A., & Deming, D. 2016, *ArXiv e-prints*, [ADS, 1612.01245](#)
- Hubeny, I., Burrows, A., & Sudarsky, D. 2003, *ApJ*, 594, 1011, [ADS, astro-ph/0305349](#)
- Kataria, T., Showman, A. P., Fortney, J. J., Stevenson, K. B., Line, M. R., Kreidberg, L., Bean, J. L., & Désert, J.-M. 2015, *ApJ*, 801, 86, [ADS, 1410.2382](#)
- Kendrew, S. et al. 2015, *PASP*, 127, 623, [ADS, 1512.03000](#)
- Knutson, H. A. et al. 2007, *Nature*, 447, 183, [ADS, 0705.0993](#)
- . 2009, *ApJ*, 690, 822, [ADS, 0802.1705](#)
- Kreidberg, L. et al. 2014, *ApJ*, 793, L27, [ADS, 1410.2255](#)
- Laraia, A. L., Gamache, R. R., Lamouroux, J., Gordon, I. E., & Rothman, L. S. 2011, *Icarus*, 215, 391, [ADS](#)
- Laughlin, G., & Lissauer, J. J. 2015, *ArXiv e-prints*, [ADS, 1501.05685](#)
- Lee, J.-M., Fletcher, L. N., & Irwin, P. G. 2012, *MNRAS*, 420, 170
- Line, M. R., Knutson, H., Wolf, A. S., & Yung, Y. L. 2014, *ApJ*, 783, 70, [ADS, 1309.6663](#)
- Line, M. R. et al. 2013, *ApJ*, 775, 137, [ADS, 1304.5561](#)
- Line, M. R., & Yung, Y. L. 2013, *ApJ*, 779, 3, [ADS, 1309.6679](#)
- Madhusudhan, N., & Seager, S. 2009, *ApJ*, 707, 24, [ADS, 0910.1347](#)
- . 2010, *ApJ*, 725, 261, [ADS, 1010.4585](#)
- Mihalas, D., Auer, L. H., & Mihalas, B. R. 1978, *ApJ*, 220, 1001, [ADS](#)
- Mollière, P., van Boekel, R., Bouwman, J., Henning, T., Lagage, P.-O., & Min, M. 2017, *A&A*, 600, A10, [ADS](#)
- Parmentier, V., & Guillot, T. 2014, *A&A*, 562, A133, [ADS, 1311.6597](#)
- Rauscher, E., & Menou, K. 2012, *ApJ*, 750, 96, [ADS, 1112.1658](#)
- Richard, C. et al. 2012, *J. Quant. Spec. Radiat. Transf.*, 113, 1276, [ADS](#)
- Rojo, P. 2006, *PhD dissertation*, Cornell University
- Rojo, P., Harrington, J., Deming, D., & Fortney, J. 2009, in *Astronomical Society of the Pacific Conference Series*, Vol. 420, *Bioastronomy 2007: Molecules, Microbes and Extraterrestrial Life*, ed. K. J. Meech, J. V. Keane, M. J. Mumma, J. L. Siefert, & D. J. Werthimer, 321, [ADS](#)
- Rothman, L. et al. 2013, *J. Quant. Spec. Radiat. Transf.*, 130, 4
- . 2010, *J. Quant. Spec. Radiat. Transf.*, 111, 2139
- Sharp, C. M., & Burrows, A. 2007, *ApJS*, 168, 140, [ADS, astro-ph/0607211](#)
- Showman, A. P., Fortney, J. J., Lian, Y., Marley, M. S., Freedman, R. S., Knutson, H. A., & Charbonneau, D. 2009, *ApJ*, 699, 564
- Southworth, J. 2010, *MNRAS*, 408, 1689, [ADS, 1006.4443](#)
- Swain, M. et al. 2013, *Icarus*, 225, 432
- Swain, M. R., Vasisht, G., & Tinetti, G. 2008, *Nature*, 452, 329, [ADS](#)
- ter Braak, C. J., & Vrugt, J. A. 2008, *Statistics and Computing*, 18, 435
- TriAUD, A. H. M. J. et al. 2009, *A&A*, 506, 377, [ADS, 0907.2956](#)
- Waldmann, I. P., Tinetti, G., Rocchetto, M., Barton, E. J., Yurchenko, S. N., & Tennyson, J. 2015, *ApJ*, 802, 107, [ADS, 1409.2312](#)
- White, W. B., Johnson, S. M., & Dantzig, G. B. 1958, *J. Chem. Phys.*, 28, 751, [ADS](#)